Exoplanets around Low-mass Stars Unveiled by K2

(article starts on next page)

https://doi.org/10.3847/1538-3881/aaa9c1

CrossMark

Exoplanets around Low-mass Stars Unveiled by *K2*

Teruyuki Hirano[1] , Fei Dai[2,3] , Davide Gandolfi[4] , Akihiko Fukui[5] , John H. Livingston[6], Kohei Miyakawa[1],
Michael Endl[7] , William D. Cochran[7] , Francisco J. Alonso-Floriano[8,9], Masayuki Kuzuhara[10,11], David Montes[9],
Tsuguru Ryu[11,12] , Simon Albrecht[13], Oscar Barragan[4], Juan Cabrera[14] , Szilard Csizmadia[14], Hans Deeg[15,16] ,
Philipp Eigmüller[14] , Anders Erikson[14], Malcolm Fridlund[8,17] , Sascha Grziwa[18] , Eike W. Guenther[19], Artie P. Hatzes[19],
Judith Korth[18], Tomoyuki Kudo[20] , Nobuhiko Kusakabe[10,11], Norio Narita[6,10,11] , David Nespral[15,16], Grzegorz Nowak[15,16] ,
Martin Pätzold[18], Enric Palle[15,16], Carina M. Persson[17], Jorge Prieto-Arranz[15,16], Heike Rauer[14,21], Ignasi Ribas[22] ,
Bun'ei Sato[1] , Alexis M. S. Smith[14], Motohide Tamura[6,10,11] , Yusuke Tanaka[6], Vincent Van Eylen[8] , and Joshua N. Winn[3]

[1] Department of Earth and Planetary Sciences, Tokyo Institute of Technology, 2-12-1 Ookayama,
Meguro-ku, Tokyo 152-8551, Japan; hirano@geo.titech.ac.jp
[2] Department of Physics, and Kavli Institute for Astrophysics and Space Research, Massachusetts Institute of Technology, Cambridge, MA 02139, USA
[3] Department of Astrophysical Sciences, Princeton University, 4 Ivy Lane, Princeton, NJ 08544, USA
[4] Dipartimento di Fisica, Universitá di Torino, via P. Giuria 1, I-10125 Torino, Italy
[5] Okayama Astrophysical Observatory, National Astronomical Observatory of Japan, Asakuchi, Okayama 719-0232, Japan
[6] Department of Astronomy, Graduate School of Science, The University of Tokyo, Hongo 7-3-1, Bunkyo-ku, Tokyo, 113-0033, Japan
[7] Department of Astronomy and McDonald Observatory, University of Texas at Austin, 2515 Speedway, Stop C1400, Austin, TX 78712, USA
[8] Leiden Observatory, Leiden University, 2333CA Leiden, The Netherlands
[9] Departamento de Astrofísica y Ciencias de la Atmósfera, Facultad de Ciencias Físicas, Universidad Complutense de Madrid, E-28040 Madrid, Spain
[10] Astrobiology Center, NINS, 2-21-1 Osawa, Mitaka, Tokyo 181-8588, Japan
[11] National Astronomical Observatory of Japan, NINS, 2-21-1 Osawa, Mitaka, Tokyo 181-8588, Japan
[12] SOKENDAI (The Graduate University for Advanced Studies), 2-21-1 Osawa, Mitaka, Tokyo 181-8588, Japan
[13] Stellar Astrophysics Centre, Department of Physics and Astronomy, Aarhus University, Ny Munkegade 120, DK-8000 Aarhus C, Denmark
[14] Institute of Planetary Research, German Aerospace Center, Rutherfordstrasse 2, D-12489 Berlin, Germany
[15] Instituto de Astrofísica de Canarias, C/Vía Láctea s/n, E-38205 La Laguna, Spain
[16] Departamento de Astrofísica, Universidad de La Laguna, E-38206 La Laguna, Spain
[17] Department of Space, Earth and Environment, Chalmers University of Technology, Onsala Space Observatory, SE-439 92 Onsala, Sweden
[18] Rheinisches Institut für Umweltforschung an der Universität zu Köln, Aachener Strasse 209, D-50931 Köln, Germany
[19] Thüringer Landessternwarte Tautenburg, Sternwarte 5, D-07778 Tautenberg, Germany
[20] Subaru Telescope, National Astronomical Observatory of Japan, 650 North Aohoku Place, Hilo, HI 96720, USA
[21] Center for Astronomy and Astrophysics, TU Berlin, Hardenbergstr. 36, D-10623 Berlin, Germany
[22] Institut de Ciències de l'Espai (CSIC-IEEC), Carrer de Can Magrans, Campus UAB, E-08193 Bellaterra, Spain

Abstract

We present the detection and follow-up observations of planetary candidates around low-mass stars observed by the *K2* mission. Based on light-curve analysis, adaptive-optics imaging, and optical spectroscopy at low and high resolution (including radial velocity measurements), we validate 16 planets around 12 low-mass stars observed during *K2* campaigns 5–10. Among the 16 planets, 12 are newly validated, with orbital periods ranging from 0.96 to 33 days. For one of the planets (K2-151b), we present ground-based transit photometry, allowing us to refine the ephemerides. Combining our *K2* M-dwarf planets together with the validated or confirmed planets found previously, we investigate the dependence of planet radius R_p on stellar insolation and metallicity [Fe/H]. We confirm that for periods $P \lesssim 2$ days, planets with a radius $R_p \gtrsim 2\,R_\oplus$ are less common than planets with a radius between 1–2 $R_\oplus$. We also see a hint of the "radius valley" between 1.5 and 2 $R_\oplus$, which has been seen for close-in planets around FGK stars. These features in the radius/period distribution could be attributed to photoevaporation of planetary envelopes by high-energy photons from the host star, as they have for FGK stars. For the M dwarfs, though, the features are not as well defined, and we cannot rule out other explanations such as atmospheric loss from internal planetary heat sources or truncation of the protoplanetary disk. There also appears to be a relation between planet size and metallicity: the few planets larger than about 3 $R_\oplus$ are found around the most metal-rich M dwarfs.

Key words: methods: observational – planets and satellites: detection – techniques: high angular resolution – techniques: photometric – techniques: radial velocities – techniques: spectroscopic

1. Introduction

M dwarfs have some advantages over solar-type (FGK) stars in the detection and characterization of transiting planets. Their smaller sizes lead to deeper transits for a given planet radius. In addition, their habitable zones occur at shorter orbital periods, facilitating the study of terrestrial planets in the habitable zone. These advantages are now widely appreciated. Many observational and theoretical studies have focused on M-dwarf planets, including their potential habitability and detectable biosignatures (e.g., Scalo et al. 2007; Shields et al. 2016). However, the number of currently known transiting planets around low-mass stars is much smaller than that for solar-type stars, because low-mass stars are optically faint. In particular, the number of mid-to-late M dwarfs ($T_{\rm eff} \lesssim 3500$ K) hosting transiting planets is extremely limited (fewer than 20, as of 2017 September). While the planets around early M dwarfs have been investigated in detail with the *Kepler* sample (Dressing &

Charbonneau 2013, 2015; Morton & Swift 2014; Mulders et al. 2015a, 2015b; Ballard & Johnson 2016), the distribution and properties of mid-to-late M-dwarf planetary systems are still relatively unexplored.

Kepler's second mission, *K2* (Howell et al. 2014), has also contributed to the search for transiting planets around M dwarfs. Hundreds of stars have been identified as candidate planet-hosting stars (e.g., Montet et al. 2015; Crossfield et al. 2016; Pope et al. 2016; Vanderburg et al. 2016), many of which have been validated (e.g., Dressing et al. 2017b). Moreover, *K2* has observed young stars in stellar clusters (e.g., the Hyades, Pleiades, and Beehive), including many low-mass stars. Several transiting planet candidates around these have already been reported (Mann et al. 2016a, 2016b, 2017b, 2018; Ciardi et al. 2017). These planets are potentially promising targets for follow-up studies such as Doppler mass measurement and atmospheric characterization.

We have been participating in *K2* planet detection and characterization in the framework of an international collaboration called KESPRINT.[23] Making use of our own pipeline to reduce the *K2* data and look for transit signals, we have detected 30–80 planet candidates in each of the *K2* campaign fields. Through intensive follow-up observations using various facilities all over the world, we have validated or confirmed many transiting planets (e.g., Sanchis-Ojeda et al. 2015; Fridlund et al. 2017; Gandolfi et al. 2017; Guenther et al. 2017). In this paper, we focus on planetary systems around M dwarfs found by the KESPRINT project.

The rest of the paper is organized as follows. In Section 2, we describe the reduction of the *K2* data and detection of the planet candidates by our pipeline. Next, we report our follow-up observations, including low- and high-resolution optical spectroscopy, high-contrast imaging, and ground-based follow-up transit observations (Section 3). Section 4 presents the analysis of the follow-up observations, through which we validate 15 planets around M dwarfs. Individual systems of special interest are described in Section 5. In Section 6, we examine the properties of all transiting planets currently known around M dwarfs, with a focus on the planetary radius. Our conclusions are in Section 7.

2. *K2* Photometry and Detection of Planet Candidates

2.1. *K2* Light-curve Reduction

Due to the loss of two of its four reaction wheels, the *Kepler* spacecraft can no longer maintain the pointing stability required to observe its original field of view. The *Kepler* telescope was repurposed for a new series of observations under the name *K2* (Howell et al. 2014). By observing in the ecliptic, the torque by solar radiation pressure is minimized, significantly improving its pointing stability. The spacecraft must also switch to a different field of view about every three months to maintain pointing away from the Sun. In this operational mode, the photometry is strongly affected by the rolling motion of the spacecraft along its boresight and the variation of pixel sensitivity. To reduce this effect, we adopted an approach similar to that described by Vanderburg & Johnson (2014).

We now briefly describe our light-curve production pipeline. We downloaded the target pixel files from the Mikulski Archive for Space Telescopes.[24] We then put down circular apertures surrounding the brightest pixel within the collection of pixels recorded for each target. We fitted a 2D Gaussian function to the intensity distribution at each recorded time. The resultant X and Y positions of the Gaussian function, as a function of time, allowed us to track the rolling motion of the spacecraft. To reduce the intensity fluctuations associated with this motion, we divided the apparent flux variation by the best-fitting piecewise linear relationship between the apparent flux and the coordinates X and Y. The systematic correction was described in more detail by Dai et al. (2017).

2.2. Transit Detection

To remove any long-term systematic or instrumental flux variations that may complicate the search for transit signals, we fitted the *K2* light curve with a cubic spline with a timescale of 1.5 days. The observed light curve was then divided by the spline fit. The smoothing interval of 1.5 days was chosen to be much longer than the expected duration of planetary transits, which are measured in hours for short-period planets around dwarf stars. We then searched for periodic transit signals with the Box Least Squares algorithm (BLS; Kovács et al. 2002). We employed a modification of the BLS algorithm, using a more efficient nonlinear frequency grid that takes into account the scaling of transit duration with orbital period (Ofir 2014). To quantify the significance of a transit detection, we adopted the signal detection efficiency (SDE; Ofir 2014), which is defined by the amplitude of peak in the BLS spectrum normalized by the local standard deviation. A signal was considered significant if the SDE is greater than 6.5. To search for any additional planets in the system, we recomputed the BLS spectrum after removing the transit signal that was detected in the previous iteration, until the maximum SDE dropped below 6.5.

2.3. Initial Vetting

After the transit signals were identified, we performed a quick initial vetting process to exclude obvious false positives. We sought evidence for any alternation in the eclipse depths or a significant secondary eclipse, either of which would reveal the system to be an eclipsing binary (EB). Such effects should not be observed if the detected signal is from a planetary transit. We fitted a Mandel & Agol (2002) model to the odd- and even-numbered transits separately. If the transit depths differed by more than 3σ, the system was flagged as a likely false positive.

We also searched for any evidence of a secondary eclipse. First, we fitted the observed transits with a Mandel & Agol (2002) model. The fit was used as a template for the secondary eclipse. We allowed the eclipse depth and time of opposition to float freely; all other relevant parameters were held fixed based on the transit model. If a secondary eclipse was detected with more than 3σ significance, we then calculated the geometric albedo implied by the depth of the secondary eclipse. If the implied albedo was much larger than 1, we concluded that the eclipsing object is likely to be too luminous to be a planet. Typically, in each of *K2* Campaigns 5, 6, 7, 8, and 10,

---

[24] https://archive.stsci.edu/k2

approximately 5–10 M-dwarf planetary candidates survived this initial vetting process.

3. Observations and Data Reductions

We here report the follow-up observations for the planet candidates around M dwarfs detected by our pipeline. The complete list of our candidates will be presented elsewhere (Livingston et al. and other papers in preparation). We attempted follow-up observations for as many M-dwarf planet hosts as possible. Our selection of targets included all planet candidates that had not already been validated (to our knowledge), with a preference for northern hemisphere targets for which our follow-up resources are best suited. Specifically, we report on the candidates around K2-117, K2-146, K2-122, K2-123, K2-147, EPIC 220187552, EPIC 220194953, K2-148, K2-149, K2-150, K2-151, K2-152, K2-153, and K2-154, for which we conducted both high-resolution imaging and optical spectroscopy. This list of M dwarfs covers about half of all candidate planet hosts in the *K2* Campaign fields 5, 8, and 10. Campaign fields 6 and 7 are located in the southern hemisphere where our telescope resources are limited. The M-dwarf systems we did not follow up are generally fainter objects ($V > 15$) for which follow-up observations are difficult and time consuming.

3.1. Low-dispersion Optical Spectroscopy

We conducted low-dispersion optical spectroscopy with the Calar Alto Faint Object Spectrograph (CAFOS) on the 2.2 m telescope at the Calar Alto observatory. We observed planet-host candidates in *K2* campaign fields 5 and 8 (K2-117, K2-146, K2-123, EPIC 220187552, EPIC 220194953, K2-149, K2-150, K2-151) on UT 2016 October 28 and 29, and three stars in field 10 (K2-152, K2-153, K2-154) on UT 2017 February 21.[25] Following Alonso-Floriano et al. (2015), we employed the grism "G-100" setup, covering $\sim$4200–8300 Å with a spectral resolution of $R \sim 1500$. The exposure times ranged from 600 to 2400 s, depending on the magnitude of each star. For long exposures (>600 s), we split the exposures into several small ones so that we can minimize the impact of cosmic rays on the data reduction. For the absolute flux calibration, we observed Feige 34 as a flux standard on each observing night. We did not observe K2-147 because this target never rises above 25° elevation at Calar Alto.

We reduced the data taken by CAFOS in a standard manner using IRAF packages: bias subtraction, flat-fielding, sky-subtraction, and extraction of one-dimensional (1D) spectra. The wavelength was calibrated using the revised line list of the comparison lamp (Hg–Cd–Ar) spectrum (Alonso-Floriano et al. 2015). Finally, we corrected the instrumental response and converted the flux counts into absolute fluxes using the extracted 1D spectrum of Feige 34. The data for one of the targets, K2-123, were not useful because the signal-to-noise ratio (S/N) of the spectrum turned out to be too low. Figure 1 plots the reduced, normalized spectra observed by CAFOS.

3.2. High-dispersion Spectroscopy

In order to estimate stellar physical parameters and check the binarity, we obtained high-resolution optical spectra with

---
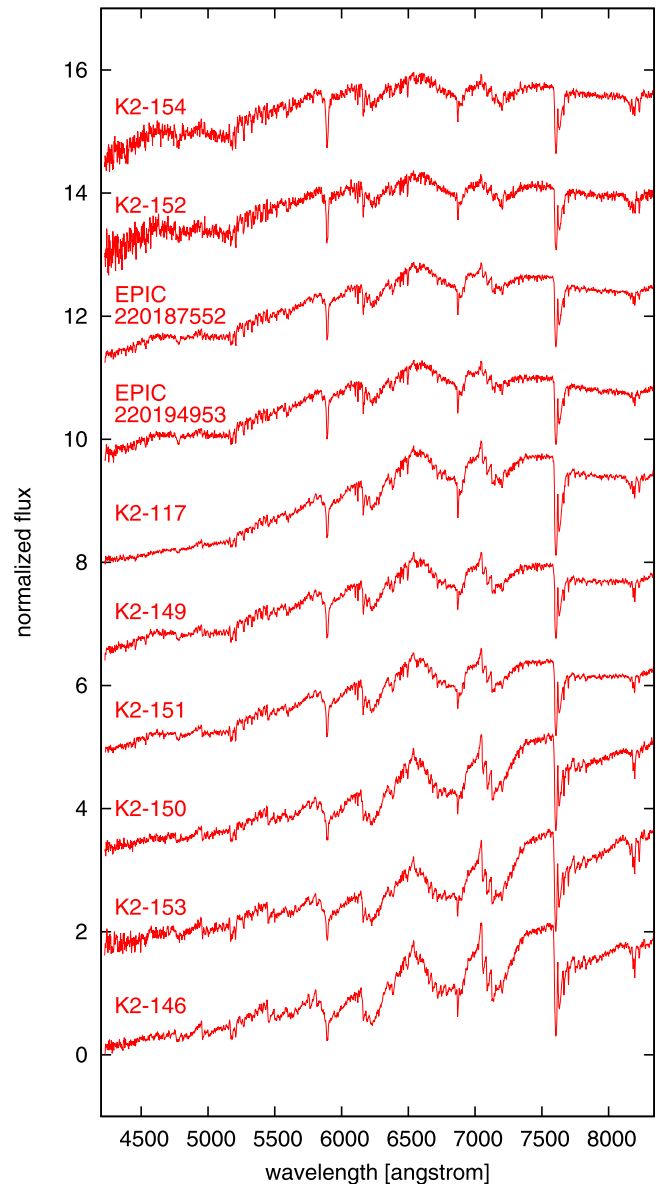
Figure 1. Wavelength-calibrated, normalized optical spectra observed by CAFOS. Later M dwarfs are plotted toward the bottom.

various spectrographs. K2-117, K2-146, K2-123, K2-147, EPIC 220187552, EPIC 220194953, K2-148, K2-149, K2-150, K2-151, and K2-153 were observed by the High Dispersion Spectrograph (HDS; Noguchi et al. 2002) on the Subaru 8.2 m telescope between the fall of 2015 and the summer of 2017. For all HDS targets except K2-146, we adopted the standard "I2a" setup and Image Slicer #2 (Tajitsu et al. 2012), covering the spectral region of $\sim$4900–7600 Å with a resolving power of $R \sim 80{,}000$. To avoid a telescope auto-guiding error, we adopted the normal slit with its width being $0\rlap{.}{''}6$ ($R \sim 60{,}000$) for K2-146, which is the faintest in the optical among our targets.

For K2-123, EPIC 220187552, K2-149, K2-150, and K2-151, we also conducted multi-epoch observations, spanning at least a few days, mainly to check the absence of large RV variations ($\gtrsim 1$ km s^{-1}) caused by stellar companions (i.e., EB scenarios). Except for K2-150, the multi-epoch spectra were taken with the iodine (I$_2$) cell; the stellar light, transmitted through the cell, is

Table 1
Results of RV Measurements

BJD$_{TDB}$ (−2450000.0)	RV (km s^{-1})	RV Error (km s^{-1})	RV Type	Instrument
K2-122				
7343.722376	−14.6049	0.0248	absolute	FIES
7395.510251	−14.6245	0.0248	absolute	FIES
7398.646686	−14.5949	0.0269	absolute	FIES
7399.624305	−14.6259	0.0276	absolute	FIES
7370.661943	−14.3411	0.0049	absolute	HARPS-N
7370.683403	−14.3435	0.0058	absolute	HARPS-N
7372.633972	−14.3511	0.0111	absolute	HARPS-N
7372.653348	−14.3610	0.0237	absolute	HARPS-N
7400.532625	−14.3494	0.0055	absolute	HARPS-N
7400.553493	−14.3447	0.0047	absolute	HARPS-N
K2-123				
7674.087730	0.0156	0.0150	relative	HDS
7675.115382	−0.0102	0.0162	relative	HDS
7676.095845	0.0245	0.0171	relative	HDS
K2-147				
7893.706393	−24.9163	0.0127	absolute	FIES
7931.617000	−24.9256	0.0122	absolute	FIES
K2-149				
7674.002138	0.0132	0.0213	relative	HDS
7675.030047	0.0034	0.0200	relative	HDS
7675.998989	−0.0346	0.0209	relative	HDS
K2-150				
7675.072056	4.748	0.171	absolute	HDS
7921.089719	4.850	0.339	absolute	HDS
K2-151				
57674.03764	0.0089	0.0115	relative	HDS
7675.094883	−0.0082	0.0114	relative	HDS
7676.077393	−0.0107	0.0129	relative	HDS
K2-152				
7834.755773	−8.153	0.133	absolute	Tull
7954.629452	−7.643	0.614	absolute	Tull

imprinted with the iodine absorption lines which are used for the simultaneous precise calibration of wavelength (e.g., Butler et al. 1996). By using the I$_2$ cell, we can improve the RV precision by more than tenfold, and cannot only rule out the EB scenario but also put a constraint on planetary masses, provided that the spectra are obtained at appropriate orbital phases. The only drawback is that we need to take one additional I$_2$-free spectrum as a template in the RV analysis for each target.

Two-dimensional (2D) HDS data in echelle format were reduced in the standard manner, including flat-fielding, scattered-light subtraction, and extraction of 1D spectra for multiple orders. The wavelength was calibrated based on the Th–Ar emission lamp spectra obtained at the beginning and end of each observing night. Typical S/Ns of the resulting 1D spectra were ∼20–50 per pixel around sodium D lines.

For RV targets observed with the I$_2$ cell (K2-123, EPIC 220187552, K2-149, and K2-151), we put the reduced 1D spectra into the RV analysis pipeline developed by Sato et al. (2002) and extracted relative RV values with respect to the I$_2$-out template spectrum for each target. Among the four targets, the RV fit did not converge for EPIC 220187552, which turns out to be a spectroscopic binary (see Sections 3.3 and 4.1). The results of RV measurements are summarized in Table 1. Figure 2 plots the relative RV variation as a function of orbital phase of each planet candidate; the absence of significant RV variations, along with the typical RV precision
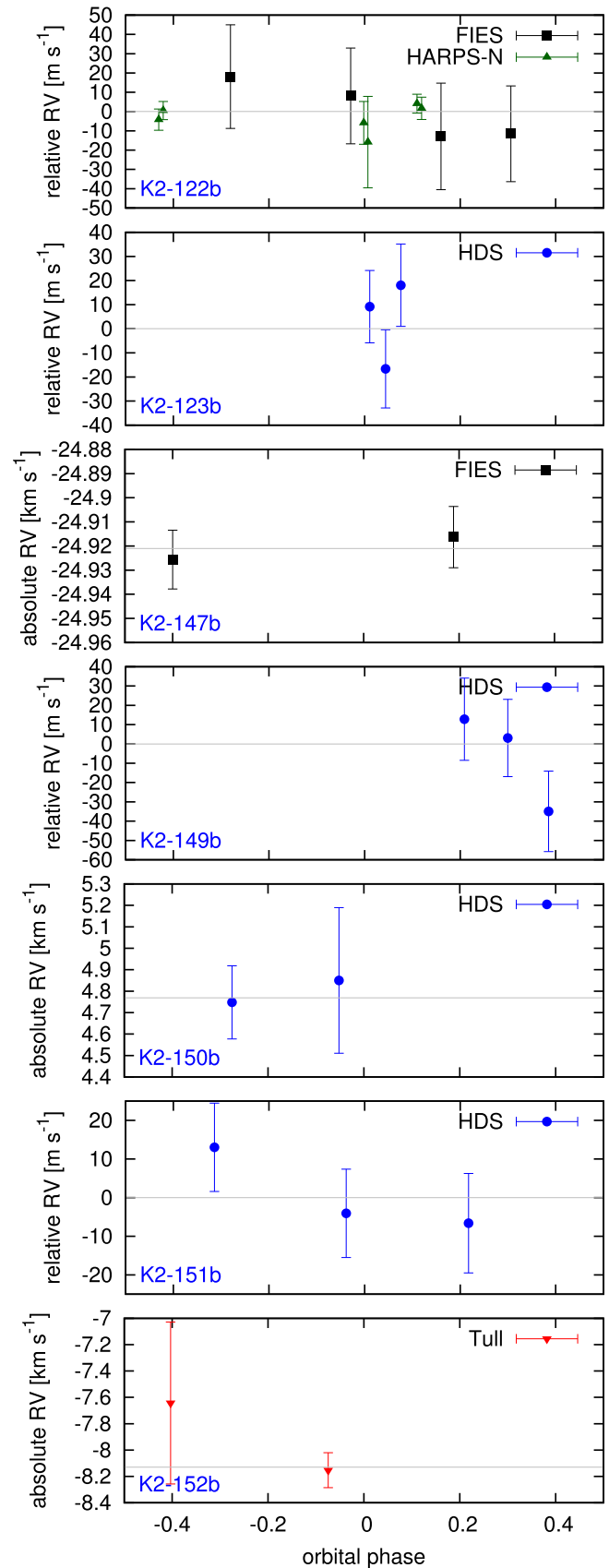
Figure 2. RV values folded by the orbital period of each transiting planet. Relative RV values are plotted for K2-122, K2-123, K2-149, and K2-151, while absolute RV values are shown for K2-147, K2-150, and K2-152. Note that for K2-122, the systemic velocity was subtracted from each data set to take into account the small RV offset between the FIES and HARPS-N data sets.

of 10–20 m s^{-1} for I$_2$-in spectra, completely rules out the presence of stellar companions in close-in orbits.

We performed RV follow-up observations of K2-122 and K2-147 using the FIbre-fed Échelle Spectrograph (FIES; Frandsen & Lindberg 1999; Telting et al. 2014) mounted at the 2.56 m Nordic Optical Telescope (NOT) of Roque de los Muchachos Observatory (La Palma, Spain). We collected four high-resolution spectra ($R \sim 67{,}000$) of K2-122 between 2015 November and 2016 January, and two intermediate-resolution spectra ($R \sim 47{,}000$) of K2-147 in 2017 May and June, as part of the observing programs P52-201 (CAT), P52-108 (OPTI-CON), and P55-019. Three consecutive exposures of 900–1200 s were secured to remove cosmic-ray hits, leading to an S/N of 25–30 per pixel at 5800 Å. We followed the observing strategy described in Buchhave et al. (2010) and Gandolfi et al. (2013), and traced the RV intra-exposure drift of the instrument by acquiring long-exposed ($T_{\rm exp} = 35$ s) Th–Ar spectra immediately before and after each observation. The data reduction was performed using standard IRAF and IDL routines, which include bias subtraction, flat-fielding, order tracing and extraction, and wavelength calibration. The RVs were determined by multi-order cross-correlation against a spectrum of the M2-dwarf GJ 411 that was observed with the same instrumental setups as the two target stars, and for which we adopted an absolute RV of -84.689 km s^{-1}.

We also acquired six high-resolution spectra ($R \sim 115{,}000$) of K2-122 using the HARPS-N spectrograph (Cosentino et al. 2012) mounted at the 3.58 m Telescopio Nazionale Galileo (TNG) of Roque de los Muchachos Observatory (La Palma, Spain). Two consecutive exposures of 1800 s were acquired at three different epochs between 2016 December and 2017 January as part of the CAT and OPTICON programs CAT15B_35 and OPT15B_64, using the second HARPS-N fiber to monitor the sky background. Unfortunately, the spectra taken on BJD = 2457372 are affected by poor sky conditions. We reduced the data using the dedicated offline pipeline. The S/N is between 5 and 20 per pixel at 5800 Å. RVs were extracted by cross-correlating the extracted echelle spectra with the M2 numerical mask (Table 1).

We observed K2-152 and K2-154 with the Harlan J. Smith 2.7 m telescope and its Tull Coudé high-resolution ($R = 60{,}000$) optical spectrograph (Tull et al. 1995) at McDonald Observatory. We obtained one reconnaissance spectrum of K2-152 in 2017 March and a second one in 2017 July. We also collected one spectrum of K2-154 in 2017 March. Exposure times ranged from 29 to 50 minutes, due to the faintness of these stars in the optical. The spectra were all bias-subtracted, flat-field divided, and extracted using standard IRAF routines. For the wavelength calibration, we use Th–Ar calibration exposures taken adjacent to the science observations. We analyzed the spectra using our Kea code (Endl & Cochran 2016) to determine stellar parameters. Kea is not well-suited to derive accurate parameters for cooler stars, but the results showed that both stars are cool ($T_{\rm eff} \sim 4000$ K) main-sequence stars. In Section 4.1.2, we will perform a more uniform analysis to estimate stellar parameters.

3.3. High-contrast Imaging

In transit surveys, typical false positives arise from background or hierarchical triple EBs. High-resolution imaging is especially useful to constrain background EB scenarios, and thus has intensively been used for planet validations (e.g., Dressing et al. 2017b). To search for nearby companions that could be the source of the observed transit-like signal, we conducted

high-resolution imaging using the adaptive-optics system (AO188; Hayano et al. 2010) with the High Contrast Instrument (HiCIAO; Suzuki et al. 2010) for K2-146 and K2-122 and the Infrared Camera and Spectrograph (IRCS; Kobayashi et al. 2000) for the other systems, both mounted on the Subaru telescope between the winter of 2015 and the summer of 2017.

For the HiCIAO observation, we adopted the same observing scheme as described in Hirano et al. (2016b), except that we employed angular differential imaging (Marois et al. 2006) for K2-146. With the three-point dithering and H-band filter, a total of 11 unsaturated frames after co-addition were obtained with AO for K2-146, resulting in the total exposure time of 1135 s. For K2-122, we obtained three saturated frames (after co-addition) with two-point dithering, corresponding to the total exposure time of 450 s. We also took two unsaturated frames for absolute flux calibration using a neutral-density filter.

HiCIAO data were reduced with the ACORNS pipeline developed by Brandt et al. (2013) for the removal of biases and correlated noises, hot pixel masking, flat-fielding, and distortion correction. We applied the distortion correction adopted in Hirano et al. (2016b), which was made using the globular cluster image following Brandt et al. (2013). We then aligned and median-combined the processed frames to obtain the highest contrast image. The resulting FWHM of the combined images was $\sim 0\rlap{.}''07$. We visually inspected the combined images for K2-146 and K2-122, and found two neighboring faint companions to the northwest of K2-146. The brighter of the two is located $9\rlap{.}''1$ away from K2-146 with $\Delta m_H = 6.7$ mag, while the fainter is $8\rlap{.}''7$ away from K2-146 with $\Delta m_H = 7.7$ mag. Checking the SDSS catalog (Ahn et al. 2012), we identified a star around the coordinate where two faint stars were detected and found its relative magnitude to be $\Delta m_r = 6.4$ mag. These faint stars are inside the photometric aperture for the $K2$ light curve, but the optical and near-infrared magnitudes imply that these cannot produce the deep transit signal detected for K2-146. We detected no nearby companion in the combined image of K2-122.

Regarding IRCS observations, we conducted AO imaging using each target itself as the natural guide for AO with the H-band filter. Adopting the fine sampling mode (1 pix = $0\rlap{.}''02057$) and five-point dithering, we ran two kinds of sequences for each target. The first sequence consists of long exposures to obtain saturated frames of the targets, which are used to search for faint nearby companions. The total exposure time varied widely for each target, but is typically ~ 360 s for an $m_H = 10$ mag star. The saturation radii were less than $0\rlap{.}''05$ for all frames. As the second sequence, we also took unsaturated frames with much shorter exposures and used these frames for absolute flux calibrations.

Following Hirano et al. (2016a), we reduced the raw IRCS data—subtraction of the dark current, flat-fielding, and distortion correction—before aligning and median-combining the frames for each target. The combined images were respectively generated for saturated and unsaturated frames. We visually checked the combined saturated image for each target, in which the field of view (FoV) is $\sim 16'' \times 16''$. Most importantly, we found that EPIC 220187552 consists of two stars of similar magnitude separated by $\sim 0\rlap{.}''3$ from each other (Figure 3). In the same image, we also found a faint star $\sim 6''$ away from EPIC 220187552 with $\Delta m_H \sim 8$ mag. EPIC 220194953 and K2-148 were both imaged in the same combined frame. K2-147's combined image also exhibits a possible faint star ($\Delta m_H \sim 9.5$ mag) in the south, but with a
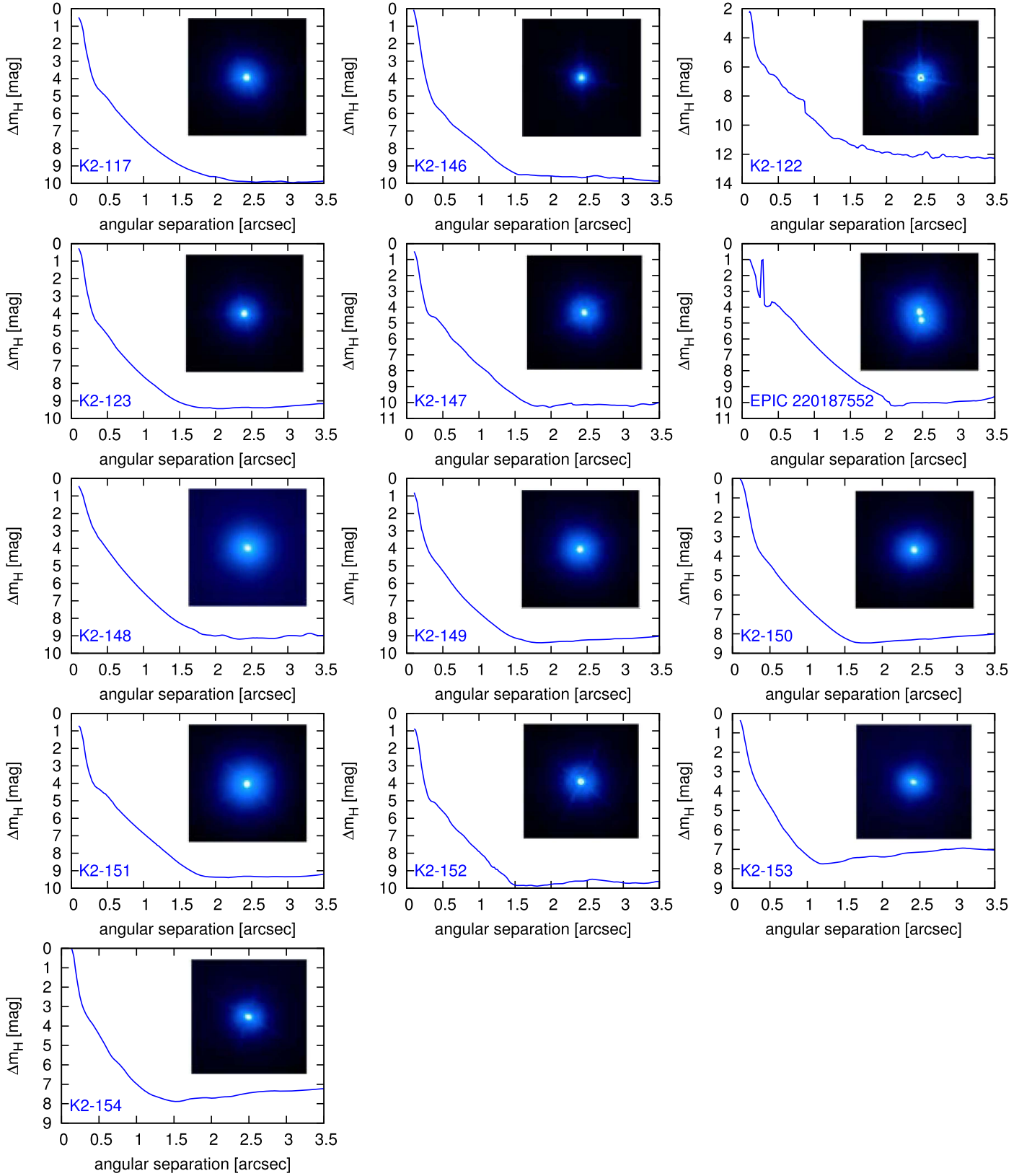
Figure 3. 5σ contrast curves in the H band as a function of angular separation from the centroid for *K2* planet-host candidates. The insets display the saturated combined images with FoV of $4'' \times 4''$. EPIC 220187552 is clearly a multiple-star system, and we conclude that the candidate is a false positive.

low S/N, separated by $4{.}''6$. We found no bright nearby stars in the FoV for the other targets.

To estimate the detection limit of faint nearby sources in the combined HiCIAO and IRCS images, we drew a 5σ contrast curve for each object. To do so, we first convolved the saturated images, with each convolution radius being half of the FWHM. We then calculated the scatter of the flux counts in the narrow annulus as a function of angular separation from the

target's centroid. Finally, we obtained the target's absolute flux by aperture photometry using the unsaturated frames for each target, with the aperture diameter being the FWHM, and normalized the flux scatter in the annulus by dividing by the photometric value after adjusting the exposure times for the saturated and unsaturated combined images. Figure 3 displays the 5σ contrast curves for all objects, along with the $4'' \times 4''$ combined images of the targets in the insets. Note that as we show in Section 4.2.1, EPIC 220194953 and K2-148 are imaged in the same frame, but since K2-148 is likely the host of transiting planets, we show the contract curve around it.

3.4. Follow-up Transit Observations

3.4.1. OAO 188 cm/MuSCAT

On 2016 September 20, we conducted a photometric follow-up observation of a transit of K2-151b with the Multi-color Simultaneous Camera for studying Atmospheres of Transiting exoplanets (MuSCAT; Narita et al. 2015) on the 1.88 m telescope at Okayama Astronomical Observatory (OAO). MuSCAT is equipped with three $1k \times 1k$ CCDs with a pixel scale of $0''\!.36$ pixel^{-1}, enabling us to obtain three-band images simultaneously through the SDSS second-generation g'-, r'-, and z_s-band filters. We set the exposure times to 60, 10, and 25 s for the g', r', and z_s bands, respectively. We observed the target star along with several bright comparison stars for ~3.8 hr, which covered well the expected ~1.5 hr duration transit. The sky was photometric except for ~0.9 hr near the end of the observation, when clouds passed; we omit the data during this period from the subsequent data reduction process. As a result, 166, 749, and 354 images were obtained in the g', r', and z_s bands, respectively, through clear skies.

The observed images were dark-subtracted, flat-fielded, and corrected for the nonlinearlity of each detector. Aperture photometry was performed with a customized pipeline (Fukui et al. 2011) for the target star and three similar-brightness stars for comparison, one of which, however, was saturated on the g'-band images and omitted from the rest of the analysis for this band. The aperture radius for each band was optimized so that the apparent dispersion of a relative light curve (a light curve of the target star divided by that of the comparison stars) was minimized. As a result, the radii of 11, 13, and 12 pixels were adopted for the g', r', and z_s bands, respectively.

3.4.2. IRSF 1.4 m/SIRIUS

On 2016 October 5 UT, we also conducted a follow-up transit observation with the Simultaneous Infrared Imager for Unbiased Survey (SIRIUS; Nagayama et al. 2003) on the IRSF 1.4 m telescope at the South African Astronomical Observatory. SIRIUS is equipped with three $1k \times 1k$ HgCdTe detectors with the pixel scale of $0''\!.45$ pixel^{-1}, enabling us to take three near-infrared images in the J, H, and K_s bands simultaneously. Setting the exposure times to 30 s with the dead time of about 8 s for all bands, we continued the observations for ~2.4 hr covering the expected transit time. As a result, 232 frames were obtained in each band.

The observed frames were analyzed in the same manner as the MuSCAT data. For the flat-fielding, we used 14, 14, and 36 twilight sky frames taken on the observing night for the J-, H-, and K_s-band data, respectively. We applied aperture photometry for the target and two comparison stars for all bands. However, we found that the brighter comparison star was saturated in the H-band data and was thus useless. With only the fainter comparison star, we could not achieve a sufficiently high photometric precision to extract the transit signal, and therefore we decided to ignore the H-band data from the subsequent analyses. We selected nine pixels as the optimal aperture radii for both J and K_s band data.

4. Data Analyses and Validation of Planet Candidates

4.1. Estimation of Spectroscopic Parameters

4.1.1. Spectral Types

Based on the low-resolution spectra obtained by CAFOS, we measured the spectral types (SpT) for the target stars. Following Alonso-Floriano et al. (2015), we measured a suite of (31) spectral indices for each CAFOS spectrum. Alonso-Floriano et al. (2015) found that five indices (TiO 2, TiO 5, PC1, VO-7912, and Color-M) among all have the best correlations with SpT, and thus we converted each of the measured five indices listed in Table 2 into SpT through the polynomials given by Alonso-Floriano et al. (2015), with revised coefficients (Alonso-Floriano 2015). We then took the weighted mean of the calculated SpT values to obtain the final value for each target and round those mean spectral types to the nearest standard subtypes (e.g., M0.0, M0.5, M1.0, ⋯), which are listed in Table 3. The scatter of the calculated SpT values from the five indices for each object is generally less than 0.5 subtype, which is comparable to the fiducial measurement error in SpT using the present method. The converted SpT values for K2-117 have a relatively large scatter (standard deviation = 0.523 subtype), which might be due to the passage of clouds or other bad weather conditions.

We also checked if the target stars are dwarf stars and not M giants by inspecting the index "Ratio C" (Kirkpatrick et al. 1991), which is a good indicator of surface gravity. As described in Alonso-Floriano et al. (2015), stars with a low surface gravity should have a value of Ratio C lower than ~1.07, but all the targets listed in Table 3 show higher Ratio C values, through which we safely conclude that those stars observed by CAFOS are all M dwarfs.

4.1.2. Atmospheric and Physical Parameters

In order to estimate the precise atmospheric and physical parameters of the target stars, we analyzed the high-resolution optical spectra obtained in Section 3.2. We made use of SpecMatch-Emp, developed by Yee et al. (2017). SpecMatch-Emp uses a library of optical high-resolution spectra for hundreds of well-characterized FGKM stars collected by the California Planet Search; it matches an observed spectrum of an unknown property to library stars, through which the best-matched spectra and their stellar parameters (the effective temperature T_{eff}, stellar radius R_s, and metallicity [Fe/H]) are found for the input spectrum while the RV shift and rotation plus instrumental line broadening are simultaneously optimized. SpecMatch-Emp is particularly useful for late-type stars, for which spectral fitting using theoretical models often has large systematics due to the imperfection of the molecular line list in the visible region.

Since SpecMatch-Emp was developed for optical spectra obtained by Keck/HIRES, we converted our spectra taken by Subaru/HDS, etc., into the same format as HIRES. To check the validity of applying SpecMatch-Emp to those spectra

Table 2
Spectral Indices by CAFOS Spectroscopy

EPIC	TiO 2	TiO 5	PC1	VO-7912	Color-M
211331236	0.826	0.662	1.037	0.998	0.752
211924657	0.641	0.423	1.157	1.072	1.045
212069861	1.061	0.998	0.935	0.980	0.556
220187552*	0.866	0.730	0.984	0.999	0.733
220194953*	0.877	0.742	0.978	0.994	0.713
220522664	0.807	0.635	1.012	1.004	0.778
220598331	0.697	0.481	1.137	1.049	1.057
220621087	0.789	0.622	1.023	1.010	0.816
201128338	0.919	0.775	0.949	0.998	0.748
201598502	0.662	0.472	1.163	1.073	1.269
228934525	0.888	0.748	0.955	0.995	0.753

Note. Starred systems do not have known planets.

taken by other instruments, for which spectral resolutions and pixel samplings are slightly different from those of HIRES, we put several spectra collected by Subaru/HDS in the past campaigns (e.g., Hirano et al. 2014) into SpecMatch-Emp and compared the outputs with literature values. Consequently, we found that the output $T_{\rm eff}$, R_s, and [Fe/H] are all consistent with the literature values within 2σ (typically within 1σ), and we justified the validity of applying SpecMatch-Emp to our new spectra.

Inputting our high-resolution spectra to SpecMatch-Emp, we obtained the stellar spectroscopic parameters. We discarded EPIC 220187552 from this analysis, since EPIC 220187552 was found to be a double (in fact triple) star revealed by the AO imaging (Section 3.3). The output parameters ($T_{\rm eff}$, R_s, and [Fe/H]) are listed in Table 3. To estimate the other stellar parameters (i.e., stellar mass M_s, surface gravity $\log g$, and luminosity L_s), we adopted the empirical formulas derived by Mann et al. (2015), who gave the empirical relations of stellar mass and radius as a function of the absolute K_s-band magnitude and [Fe/H]. Assuming that SpecMatch-Emp's output parameters follow independent Gaussians with their σ being the errors returned by SpecMatch-Emp, we performed Monte Carlo simulations and converted $T_{\rm eff}$, R_s, and [Fe/H] into M_s, $\log g$, and L_s through the absolute K_s-band magnitude. Those estimates are also summarized in Table 3. In the same table, we also list the distance d calculated from the apparent and absolute K_s-band magnitudes.

4.1.3. Cross-correlation Analysis

In addition to estimating stellar parameters from the high-resolution spectra, we also analyzed the line profile for each target. In the case when a transit-like signal is caused by an eclipsing spectroscopic binary of similar size, we expect to see a secondary line or distortion of the profile in the spectra, depending on the orbital phase of the binary. Using the cross-correlation technique, we computed the averaged spectral line profiles so that we can check for the presence of line blending. In doing so, we cross-correlated each observed spectrum (without the I_2 cell) with the numerical binary mask (M2 mask; see, e.g., Bonfils et al. 2013) developed for the RV analysis of HARPS-like spectrographs. From each observed spectrum, we extracted the spectral segments whose wavelengths are covered by the binary mask, and cross-correlated each segment with the mask as a function of Doppler shift (RV). We then took a

weighted average of the cross-correlation profiles to get the normalized line profile for each object.

Figure 4 displays the line profiles for the observed stars. For the targets with multi-epoch observations, we show the cross-correlation profiles with the highest S/N. Except for EPIC 220187552, all stars exhibit single-line profiles, though the cross-correlation continuum looks noisier for particularly cool stars (K2-146 and K2-150), which is most likely due to the more complicated molecular absorption features. EPIC 220187552 clearly shows the secondary line in the cross-correlation profile, as we expected from Figure 3; due to the small angular separation ($\sim0\rlap.{''}3$), the fluxes from the two stars both entered the spectrograph during our HDS observation. The difference in positions of the two lines implies that the two stars have a relative Doppler shift to each other, suggesting that either of the two has a stellar companion that is most likely responsible for the transit-like signal detected in the $K2$ light curve. Therefore, we concluded that EPIC 220187552 is a hierarchical triple system, in which two stars among the three are an EB. We will revisit this system in Section 5.

From the cross-correlation profile, we also measured the absolute RV for each target. Since Subaru/HDS (without the I_2 cell) and McDonald 2.7 m/Tull are neither stabilized spectrographs nor do they obtain simultaneous reference spectra like HARPS/HARPS-N, it is difficult to trace the small wavelength drift during a night, which prohibits accurate RV measurements. In order to correct for the wavelength drift of each spectrum, we extracted the spectral segment including strong telluric absorption lines (primarily 6860–6920 Å), and cross-correlated it against a theoretical telluric transmission spectrum at the summit of Maunakea, generated using a line-by-line radiative transfer model (LBLRTM; Clough et al. 2005). Stellar RVs and wavelength drifts are measured by inspecting the peaks (bottoms) of the cross-correlation profiles for the stellar and telluric segments, respectively. The final RV values (Table 1) are recorded by subtracting the two RV values. Note that the resulting wavelength drift is typically less than $0.5\,{\rm km\,s^{-1}}$ (less than half a pixel for HDS). Regarding K2-150 and K2-152, we obtained multiple spectra for absolute RV measurements, which are plotted in Figure 2 as a function of the candidates' phase; no significant RV variation is seen for both objects.

4.2. Light-curve Analysis

4.2.1. Fitting K2 Light Curves

In order to estimate the most precise parameters of each planet candidate, we compared the light curves for the same objects produced by three different pipelines: our own light curves (Section 2.1), ones by Vanderburg & Johnson (2014), and ones by EVEREST (Luger et al. 2016, 2017). As a result, we found that for our sample, the EVEREST light curves generally provided the best precision in terms of the scatter of the baseline flux. We thus used EVEREST light curves to estimate the final transit parameters. For the three targets in $K2$ field 10, since EVEREST light curves have not been published yet, we employed the light curves by Vanderburg & Johnson (2014).

We reduced the light curves in the following steps. First, using the reduced light-curve products, we split each target's light curve into segments, each spanning six to nine days, and detrended each segment by fitting it with a fifth-order

Table 3
Stellar Parameters by Optical Low- and High-resolution Spectroscopy

EPIC	K2 ID	SpT	T_{eff} (K)	[Fe/H] (dex)	R_s ($M_\odot$)	M_s ($M_\odot$)	$\log g$ (dex)	L_s ($L_\odot$)	d (pc)
211331236	K2-117	M1.0V	3676 ± 70	−0.22 ± 0.12	0.513 ± 0.051	0.532 ± 0.056	4.747 ± 0.046	0.044 ± 0.009	100 ± 14
211924657	K2-146	M3.0V	3385 ± 70	−0.02 ± 0.12	0.350 ± 0.035	0.358 ± 0.042	4.906 ± 0.041	0.015 ± 0.003	86 ± 11
212006344	K2-122	⋯	3903 ± 70	0.37 ± 0.12	0.612 ± 0.061	0.644 ± 0.061	4.677 ± 0.051	0.079 ± 0.017	74 ± 11
212069861	K2-123	⋯	3880 ± 70	−0.02 ± 0.12	0.592 ± 0.059	0.615 ± 0.060	4.686 ± 0.049	0.072 ± 0.016	156 ± 24
213715787	K2-147	⋯	3672 ± 70	0.19 ± 0.12	0.554 ± 0.055	0.583 ± 0.059	4.720 ± 0.048	0.051 ± 0.011	88 ± 13
220187552*	⋯	M0.5V	⋯	⋯	⋯	⋯	⋯	⋯	⋯
220194953*	⋯	M0.5V	3854 ± 70	−0.04 ± 0.12	0.575 ± 0.058	0.598 ± 0.059	4.699 ± 0.049	0.066 ± 0.014	121 ± 18
220194974	K2-148	⋯	4079 ± 70	−0.11 ± 0.12	0.632 ± 0.063	0.650 ± 0.061	4.653 ± 0.051	0.101 ± 0.022	121 ± 19
220522664	K2-149	M1.0V	3745 ± 70	0.11 ± 0.12	0.568 ± 0.057	0.595 ± 0.059	4.707 ± 0.048	0.049 ± 0.011	118 ± 18
220598331	K2-150	M2.5V	3499 ± 70	0.09 ± 0.12	0.436 ± 0.044	0.457 ± 0.051	4.822 ± 0.043	0.026 ± 0.006	110 ± 15
220621087	K2-151	M1.5V	3585 ± 70	−0.32 ± 0.12	0.429 ± 0.043	0.440 ± 0.050	4.820 ± 0.043	0.028 ± 0.006	62.7 ± 8.8
201128338	K2-152	M0.0V	3940 ± 70	0.09 ± 0.12	0.631 ± 0.063	0.654 ± 0.061	4.657 ± 0.051	0.087 ± 0.019	112 ± 18
201598502	K2-153	M3.0V	3720 ± 70	−0.26 ± 0.12	0.495 ± 0.050	0.512 ± 0.055	4.761 ± 0.045	0.043 ± 0.009	126 ± 18
228934525	K2-154	M0.0V	3978 ± 70	0.19 ± 0.12	0.649 ± 0.065	0.672 ± 0.061	4.645 ± 0.052	0.096 ± 0.021	133 ± 21

Note. Starred systems do not have planets.

polynomial to get a normalized light curve. Then, based on the preliminary ephemerides obtained in Section 2, we further extracted small segments around transit signals, in which the baseline spans 2.5 times the duration of the transit toward both sides from the transit center for each planet candidate. These light-curve segments around transits were simultaneously fitted for each planet candidate.

We fitted all of the light-curve segments simultaneously to obtain the global transit parameters as well as check possible transit timing variations (TTVs). The global transit parameters are the scaled semimajor axis a/R_s, transit impact parameter b, limb-darkening coefficients u_1 and u_2 for the quadratic law, and planet-to-star radius ratio R_p/R_s. We fixed the orbital eccentricity at $e = 0$. In addition to these, we introduced the parameters describing the flux baseline, for which we adopted a linear function of time, and the time of the transit center T_c for each transit (segment). To take into account the long cadence of the $K2$ observation, we integrated the transit model by Ohta et al. (2009) over 29.4 minutes to compare the model with observations.

Following Hirano et al. (2015), we first minimized the χ^2 statistic by Powell's conjugate direction method (e.g., Press et al. 1992) to obtain the best-fit values for all of the parameters, and fixed the baseline parameters for each segment at these values. We then implemented Markov Chain Monte Carlo (MCMC) simulations to estimate the posterior distribution of the remaining fitting parameters. We imposed Gaussian priors on $u_1 + u_2$ and $u_1 - u_2$ based on the theoretical values by Claret et al. (2013); the central values for u_1 and u_2 were derived by interpolation for each target using the stellar parameters listed in Table 3, and we adopted the dispersion of Gaussians as 0.1. At first we assigned an uncertainty to each $K2$ data point equal to the observed scatter in neighboring flux values, which sometimes led to a very small or large reduced χ^2, presumably due to non-stationary noise. To obtain reasonable uncertainties in the fitted parameter values, we rescaled the flux uncertainties such that the reduced χ^2 was equal to unity, before performing the MCMC analysis. We adopted the median, and 15.87th and 84.13th percentiles of the marginalized posterior distribution as the central value and its ±1σ for each fitting parameter.
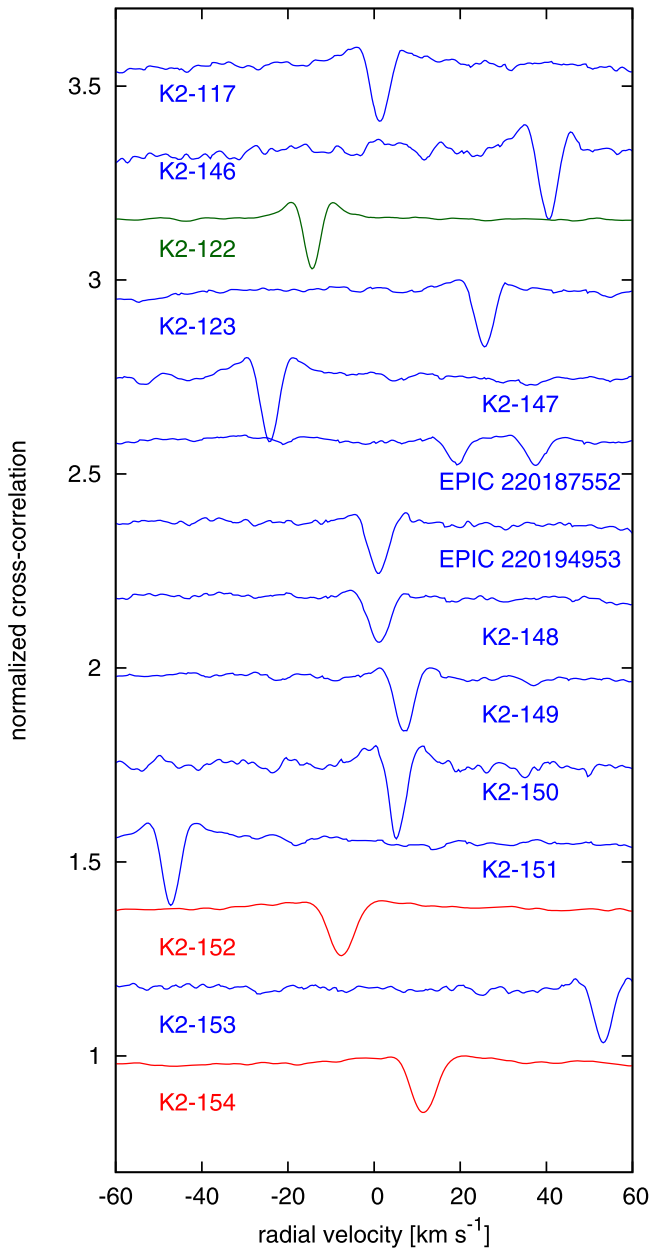
EPIC 220194953 and K2-148 are separated by ∼9″.4, and the photometric apertures used to produce EVEREST light curves for those objects involve at least a part of both stars. In order to identify which of the two stars is the source of transit signals, we analyzed three different light curves provided by EVEREST: the EVEREST version 2.0 light curves for K2-148 (EPIC 220194974) (A) and EPIC 220194953 (B), and the EVEREST version 1.0 light curve for EPIC 220194953 (C). The apertures used to produce the three light curves are shown in the central panel of Figure 5. As a result of analyzing and fitting each light curve folded by the period of K2-148c, we found that light curves based on apertures A and B exhibit similar depths in the folded transits, but the one with aperture C shows a much shallower transit (almost invisible; Figure 5). Since a significant fraction of light from K2-148 (EPIC 220194974) is missing for aperture C, K2-148 is likely the host of the transiting planet candidates.[26] We thus performed the further analysis below based on this assumption. Note that we found a similar trend when the light curve was folded by the period of K2-148b, but with a lower S/N.

To estimate the planetary parameters for K2-148b to K2-148d, we need to know the contamination (dilution) factor from EPIC 220194953 for the photometric aperture we adopt. In doing so, we estimated the flux ratio between EPIC 220194953 and K2-148 in the *Kepler* (Kp) band with the following procedure.[27] Adopting the PHOENIX atmosphere model (BT-SETTL; Allard et al. 2013), we first computed the absolute fluxes by integrating the grid PHOENIX spectra for $T_{eff} = 3600, 3700, 3800, 3900, 4000, 4100, 4200, 4300$ K over the Kp band. We then performed a Monte Carlo simulation, in which T_{eff} and R_s were randomly perturbed for both of EPIC 220194953 and K2-148 assuming Gaussian distributions based on the values in Table 3, and absolute fluxes were interpolated and converted into the photon count ratio between the two stars. Consequently, we found that the relative flux contribution from EPIC 220194953 is 0.367 ± 0.075 while that of K2-148 is 0.633 ± 0.075 in the Kp band.

---

[26] We also analyzed our own light curves using customized apertures with smaller numbers of pixels, but the transit signals became invisible owing to the larger scatter in flux.
[27] The Kp magnitudes are reported to be 12.856 and 12.975 for EPIC 220194953 and K2-148, respectively. However, the $K2$ pixel image (Kp band) and our AO image by IRCS (Figure 5; H band) both imply that K2-148 is brighter than EPIC 220194953, suggesting EPIC 220194953 is a later-type star than K2-148, and the reported Kp magnitudes are inaccurate.

contributions for aperture A as 0.357 ± 0.077 and 0.643 ± 0.077 for EPIC 220194953 and K2-148, respectively. In fitting the transit light curve, we took this dilution factor into account for K2-148.

After fitting the light-curve segments for each planet candidate, we obtained the transit parameters summarized in Table 4. Figure 6 plots the folded *K2* data around the transits (black points) along with the best-fit light-curve models (red solid lines) for individual planet candidates. For K2-117, double transit events, in which two planets transit the host star simultaneously, were predicted and identified in two light-curve segments, and we fitted these segments separately with only T_c and baseline coefficients floating freely (Figures 7 and 8). Using the optimized T_c data sets, we fitted the observed T_c for each candidate with a linear ephemeris and estimated the orbital period P and transit-center zero point $T_{c,0}$, which are also listed in Table 4. We note that in Figure 6, the data for some of the planet candidates exhibit a larger scatter in the residuals during the transits, compared to the data outside of transits. This increased scatter during transits could be ascribed to spot crossings for relatively active stars (e.g., Sanchis-Ojeda & Winn 2011), but the large outliers are probably the instrumental artifacts and were clipped in the light-curve analysis. In order to check the absence/presence of TTVs, we plot the observed minus calculated $(O - C)$ diagrams of T_c for each candidate in Figures 9–12. Visual inspection suggests that K2-146 exhibits a strong TTV while the other candidates show no clear sign of TTVs. Based on the stellar and transit parameters, we also estimate the planet radius R_p, semimajor axis a, and insolation flux from the host star S, as also shown in Table 4.
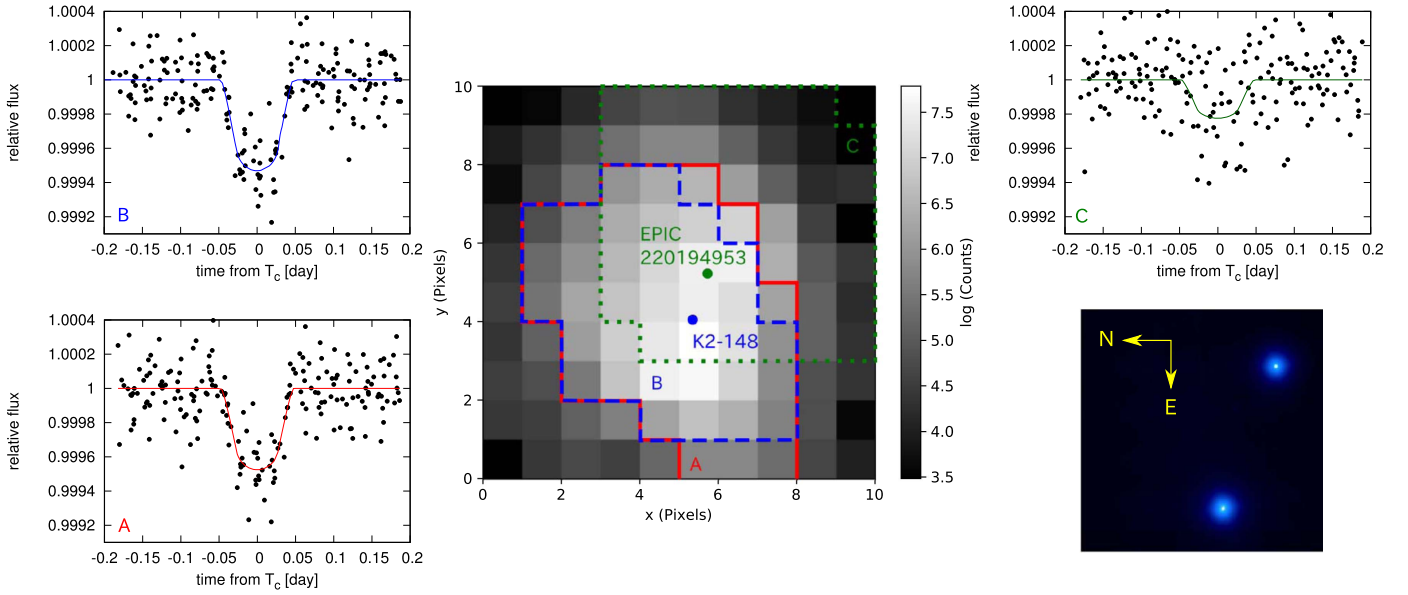
4.2.2. Fitting Ground-based Transits

Because the transit signals of K2-151b are difficult to detect in the ground-based light curves, not all transit parameters can be constrained from these light curves alone. We therefore fitted these light curves by fixing a/R_s and b at the values determined from the *K2* light curves. We also fixed the limb-darkening parameters at the theoretical values of $(u_1, u_2) = (0.37, 0.40), (0.33, 0.41), (0.45, 0.12), (0.02, 0.37),$ and $(-0.01, 0.26)$ for the g', r', z_s, J, and K_s bands, respectively. For each transit, we fitted the multiband data simultaneously by allowing the R_p/R_s for each band and a common T_c to be free. In addition, we simultaneously modeled the baseline systematics adopting a parameterization introduced by Fukui et al. (2016), which takes account of the second-order extinction effect. The applied function is

$$m_t(t) = M_{tr} + k_0 + k_t t + k_c m_c(t) + \Sigma k_i X_i, \qquad (1)$$

where m_t and m_c are the apparent magnitudes of the target star and comparison stars, respectively, M_{tr} is a transit model in magnitude scale, t is time, X_i is auxiliary observables such as stellar displacements on the detectors, sky backgrounds, and FWHM of the stellar PSFs, and k_0, k_t, k_c, and k_i are coefficients to be fitted. For the auxiliary observables, we included only the ones that show apparent correlations with the light curves; the stellar displacements in the X direction and sky backgrounds (in magnitude scale) were included for the J-band light curve and none was included for the other light curves.

To obtain the best estimates and uncertainties of the free parameters, we performed an MCMC analysis using a custom code (Narita et al. 2013). We first optimized the free parameters

Figure 4. Averaged and normalized cross-correlations between the observed spectra and M2 binary mask. Cross-correlations based on the HDS, HARPS-N, and Tull spectra are shown in blue, green, and red, respectively. The Earth's motion is corrected, and the RV value is given with respect to the barycenter of the solar system.

The actual flux contribution from each star depends on which aperture we use. We used aperture A for the light-curve fitting (Figure 5). In order to estimate the relative contributions from EPIC 220194953 and K2-148 for this aperture, we summed the total flux counts in the postage stamp (N_{tot}), the counts in the pixels in the upper half of the postage stamp which are "not" in the aperture (N_1), and the counts in the pixels in the lower half of the postage stamp which are not in the aperture (N_2). The resulting ratios N_1/N_{tot} and N_2/N_{tot} can approximately be considered as the relative flux ratios from EPIC 220194953 and K2-148 that are not inside the photometric aperture. Therefore, by subtracting these ratios from the intrinsic flux ratios above (0.367 and 0.633) and renormalizing them, we finally obtained the relative flux

Figure 5. EVEREST light curves (left panels and top-right panel) produced by different apertures (central panel) for EPIC 220194953 and K2-148 (EPIC 220194974). The light curves are folded by the period of K2-148c (=6.92 days). The right bottom panel shows a high-resolution image with an FoV of $15'' \times 15''$ taken by Subaru/IRCS; the upper-right and lower-left stars correspond to EPIC 220194953 and K2-148, respectively.

using the AMOEBA algorithm (Press et al. 1992), and rescaled the error bar of each data point so that the reduced χ^2 becomes unity. To take into account the approximate time-correlated noises, we further inflated each error bar by a factor β, which is the ratio of the standard deviation of a binned residual light curve to the one expected from the unbinned residual light curve assuming white noises alone (Pont et al. 2006; Winn et al. 2008). We then implemented 10 and 50 independent MCMC runs with 10^6 steps each for the MuSCAT and SIRIUS data, respectively, and calculated the median and 16th (84th) percentile values from the merged posterior distributions of the individual parameters. The resultant values are listed in Table 5, and the systematics-corrected light curves along with the best-fit transit models are shown in Figures 13 and 14.

We note that the detections of these transit signals are marginal. The χ^2 improvement by the best-fit transit model over a null-transit one (R_p/R_s are forced to be zero) for the MuSCAT data is 58.7, to which 6.4, 37.8, and 14.5 are contributed by the g'-, r'-, and z_s-band data, respectively, corresponding to the 6.5σ significance given the number of additional free parameters of four. In the same way, the χ^2 improvement for the SIRIUS data is 24.2, to which 15.6 and 6.6 are contributed by the J- and K_s-band data, respectively, corresponding to the 4.2σ significance given the number of additional free parameters of three. Nevertheless, as discussed below, all of the R_p/R_s values are largely consistent with each other, and all of the T_c values are well aligned, both supporting the fact that these transit detections are positive.

Based on the results of the ground-based transit observations, we compare the transit depths in different bandpasses. In Figure 15, the R_p/R_s value for each band is plotted as a function of wavelength. The blue horizontal line indicates the R_p/R_s in the Kp band, for which the $\pm 1\sigma$ errors are shown by the blue shaded area. The transit depths in the g', r', z_s, and K_s bands are consistent with the K2 result within 2σ, while the J-band result exhibits a moderate disagreement. But as is seen in Figure 13, the J-band light curve seems to suffer from a systematic flux variation, which has not been corrected by our light-curve

modeling. A more sophisticated light-curve analysis using, e.g., Gaussian processes (see, e.g., Evans et al. 2015) may be able to settle this issue.

In the absence of the follow-up transit observations, we obtained the orbital period to be $P = 3.83547 \pm 0.00015$ days from the K2 data alone. Our ground-based transit observations were conducted >180 days after the K2 observation for campaign 8 was over, as shown in Figure 16. These follow-up observations improved the precision in the orbital period of K2-151b by a factor of >6. Figure 16 also implies that the mid-transit times observed by K2 are consistent with the follow-up transit observations, and no clear sign of TTV is seen for K2-151b.

4.3. Validating Planets

We used the open source vespa software package (Morton 2015b) to compute the false positive probabilities (FPPs) of each planet candidate. Similar to previous statistical validation frameworks (Torres et al. 2011; Díaz et al. 2014), vespa relies upon Galaxy model stellar population simulations to compute the likelihoods of both planetary and non-planetary scenarios given the observations. In particular, vespa uses the TRILEGAL Galaxy model (Girardi et al. 2005) and considers false positive scenarios involving EBs, background EBs (BEBs), as well as hierarchical triple systems (HEBs). vespa models the physical properties of the host star, taking into account broadband photometry and spectroscopic stellar parameters using isochrones (Morton 2015a), and compares a large number of simulated scenarios to the observed phase-folded light curve. Both the size of the photometric aperture and contrast curve constraints are accounted for in the calculations, as well as any other observed constraints such as the maximum depth of secondary eclipses allowed by the data. Finally, vespa computes the FPP for a given planet candidate as the posterior probability of all non-planetary scenarios.

Inputting all available information (e.g., folded K2 light curves, contrast curves from AO imaging, constraint on the

Table 4
Planetary Parameters

Planet	FPP	P (days)	$T_{c,0}$ (BJD–2454833)	a/R_s	R_p/R_s	R_p ($R_\oplus$)	a (au)	S ($S_\oplus$)
K2-117b	4.5×10^{-6}	1.291563 ± 0.000026	2305.90021 ± 0.00082	$9.4^{+0.4}_{-0.5}$	$0.0362^{+0.0008}_{-0.0007}$	$2.03^{+0.21}_{-0.21}$	0.0188 ± 0.0007	123.6 ± 28.2
K2-117c	$<10^{-6}$	5.44425 ± 0.00032	2305.12220 ± 0.00208	$19.7^{+2.0}_{-4.0}$	$0.0347^{+0.0018}_{-0.0013}$	$1.94^{+0.22}_{-0.21}$	0.0491 ± 0.0017	18.1 ± 4.1
K2-146b	$<10^{-6}$	2.644646 ± 0.000043	2306.35327 ± 0.00085	$15.5^{+0.9}_{-2.5}$	$0.0577^{+0.0021}_{-0.0012}$	$2.20^{+0.23}_{-0.23}$	0.0266 ± 0.0010	20.7 ± 4.8
K2-122b	1.9×10^{-5}	2.219315 ± 0.000074	2306.60981 ± 0.00125	$13.6^{+1.3}_{-3.2}$	$0.0183^{+0.0021}_{-0.0007}$	$1.22^{+0.17}_{-0.13}$	0.0288 ± 0.0009	95.7 ± 21.5
K2-123b	1.2×10^{-4}	30.9542 ± 0.0022	2283.53953 ± 0.00476	$61.6^{+6.4}_{-15.3}$	$0.0413^{+0.0015}_{-0.0015}$	$2.66^{+0.33}_{-0.28}$	0.1641 ± 0.0053	2.7 ± 0.6
K2-147b	1.0×10^{-4}	0.961917 ± 0.000026	2468.94616 ± 0.00125	$8.8^{+1.4}_{-2.1}$	$0.0229^{+0.0016}_{-0.0011}$	$1.38^{+0.17}_{-0.15}$	0.0159 ± 0.0005	200.1 ± 45.7
K2-148b	3.7×10^{-6}	4.38395 ± 0.00080	2557.05956 ± 0.00961	$16.7^{+3.2}_{-4.5}$	$0.0193^{+0.0018}_{-0.0019}$	$1.33^{+0.19}_{-0.18}$	0.0454 ± 0.0014	48.8 ± 11.0
K2-148c	5.3×10^{-5}	6.92260 ± 0.00070	2554.72777 ± 0.00458	$27.3^{+3.6}_{-6.9}$	$0.0251^{+0.0025}_{-0.0021}$	$1.73^{+0.24}_{-0.21}$	0.0616 ± 0.0019	26.5 ± 6.0
K2-148d	1.5×10^{-4}	9.7579 ± 0.0010	2553.34305 ± 0.00545	$36.3^{+6.0}_{-9.6}$	$0.0238^{+0.0026}_{-0.0020}$	$1.64^{+0.24}_{-0.21}$	0.0774 ± 0.0024	16.8 ± 3.8
K2-149b	$<10^{-6}$	11.3320 ± 0.0013	2555.33834 ± 0.00600	$34.3^{+3.7}_{-7.9}$	$0.0264^{+0.0018}_{-0.0012}$	$1.64^{+0.20}_{-0.18}$	0.0830 ± 0.0027	7.0 ± 1.6
K2-150b	1.5×10^{-5}	10.59357 ± 0.00084	2558.96158 ± 0.00392	$32.2^{+3.6}_{-9.5}$	$0.0420^{+0.0038}_{-0.0012}$	$2.00^{+0.27}_{-0.21}$	0.0727 ± 0.0027	4.9 ± 1.1
K2-151b	1.8×10^{-6}	3.835592 ± 0.000023	2558.40166 ± 0.00104	$18.4^{+2.1}_{-5.0}$	$0.0289^{+0.0019}_{-0.0010}$	$1.35^{+0.16}_{-0.14}$	0.0365 ± 0.0014	20.8 ± 4.8
K2-152b	2.0×10^{-6}	32.6527 ± 0.0035	2742.96234 ± 0.00479	$56.9^{+5.0}_{-13.2}$	$0.0408^{+0.0029}_{-0.0015}$	$2.81^{+0.34}_{-0.30}$	0.1735 ± 0.0054	2.9 ± 0.7
K2-153b	7.3×10^{-5}	7.51554 ± 0.00098	2747.91718 ± 0.00524	$24.2^{+3.5}_{-7.2}$	$0.0371^{+0.0030}_{-0.0019}$	$2.00^{+0.26}_{-0.22}$	0.0601 ± 0.0021	11.8 ± 2.7
K2-154b	4.3×10^{-6}	3.67635 ± 0.00017	2748.37866 ± 0.00202	$13.4^{+1.5}_{-4.7}$	$0.0315^{+0.0042}_{-0.0012}$	$2.23^{+0.37}_{-0.24}$	0.0408 ± 0.0012	57.5 ± 12.9
K2-154c	1.5×10^{-6}	7.95478 ± 0.00063	2743.38098 ± 0.00350	$25.3^{+2.2}_{-5.3}$	$0.0297^{+0.0019}_{-0.0012}$	$2.10^{+0.25}_{-0.23}$	0.0683 ± 0.0021	20.5 ± 4.6

depths of secondary eclipses, and spectroscopic parameters of the target stars) from our follow-up observations and analyses, we ran `vespa` and calculated FPP for each planet candidate. Table 4 summarizes thus derived FPP for our planet candidates; all of the FPP values are well below the fiducial criterion of planet validation (FPP < 1%), by which the planet candidates listed in Table 4 are statistically validated.

AO observations by Subaru/IRCS and HiCIAO allowed us to obtain high-resolution images of candidate planet hosts, but our imaging can only cover the FoV of ∼20″ × 20″. Moreover, the targets were not imaged at the exact center of the detector, and nearby stars within *K2* photometric apertures may be missing in our high-resolution images. In order to ensure that such missing stars are not sources of false positives (i.e., BEBs), we checked the archived catalogs (e.g., Zacharias et al. 2005; Ahn et al. 2012) to look for faint nearby sources for each target. As a consequence, we found that K2-146, K2-147, K2-148, and K2-150 have nearby faint stars, which could be inside the *K2* photometric apertures (∼30″ × 30″).[28] The delta magnitudes of these nearby stars are larger than $\Delta m_r = 5$ mag, but smaller than those corresponding to the observed transit depths. Among the four systems, however, the nearby stars around K2-146, K2-148, and K2-150 are located around the edge of the *K2* photometric apertures (separation larger than 10″), and so a significant fraction of light from those faint stars should be missing in the *K2* photometry (>40%). Given this loss of light, we found it almost impossible to account for the observed transit depths even for the maximum occultation case (i.e., 50% loss of light during eclipses).

Concerning K2-147, we identified two faint sources around the target, which are separated by 10″5 ($\Delta m_R = 6.1$ mag) and 10″8 ($\Delta m_R = 6.7$ mag), respectively. Given the observed transit depth of ∼0.06%, either of these faint stars could be the source of the observed signal. To prove that this is not the case, we created new *K2* light curves using customized apertures for this object, which excluded the pixels around those faint stars. This analysis revealed that the transits are indeed reproduced

even after excluding these faint stars, by which we concluded that K2-147 is the source of transits.

Finally, we checked if the stellar densities estimated via transit fitting are consistent with the spectroscopically estimated densities, in order to make sure that the planets are indeed transiting the low-mass host stars. As a result, we found that the stellar densities from the transit modeling all have supersolar densities, suggesting that the planets are transiting low-mass stars and are in good agreement with spectroscopic values within 1σ except K2-117b, for which the two densities are compatible within 2σ. Based on all these facts above as well as the `vespa` calculations and absence of large RV variations for a fraction of systems, we conclude that the candidates in Table 4 are all bona fide planets.[29]

5. Individual Systems

5.1. K2-117

The planet candidate K2-117b ($P = 1.29$ days, $R_p = 2.03\,R_\oplus$) was first reported by Pope et al. (2016), and recently, Dressing et al. (2017b) validated this candidate along with the additional planet K2-117c of similar size ($R_p = 1.94\,R_\oplus$), orbiting the same star with $P = 5.44$ days. We report here independent validations of these planets using our own observational data (AO and a high-resolution spectrum), and have performed a more thorough analysis, including the double transit modeling (Figures 7 and 8) and TTV analysis. As shown in Figure 9, no clear TTV signals are seen in the $O - C$ diagram. The two planets exhibit moderate transit depths (∼0.15%), enabling transit follow-up observations from the ground, by which we can refine transit parameters and ephemerides.

5.2. K2-146

K2-146 is the coolest star in our sample, for which we obtain $T_{\rm eff} = 3385$ K. Pope et al. (2016) and Dressing et al. (2017b) reported that K2-146 hosts a mini-Neptune candidate in a 2.645

---

[28] Here, the faint star around K2-146 is different from the two faint sources that we identified in the HiCIAO image. The faint nearby source around K2-148 is also different from EPIC 220194953.

[29] We note that false positives of an instrumental origin are very unlikely, since our candidates do not include one whose period is close to the known periods associated with instrumental artifacts (e.g., the 6 hr rolling motion).
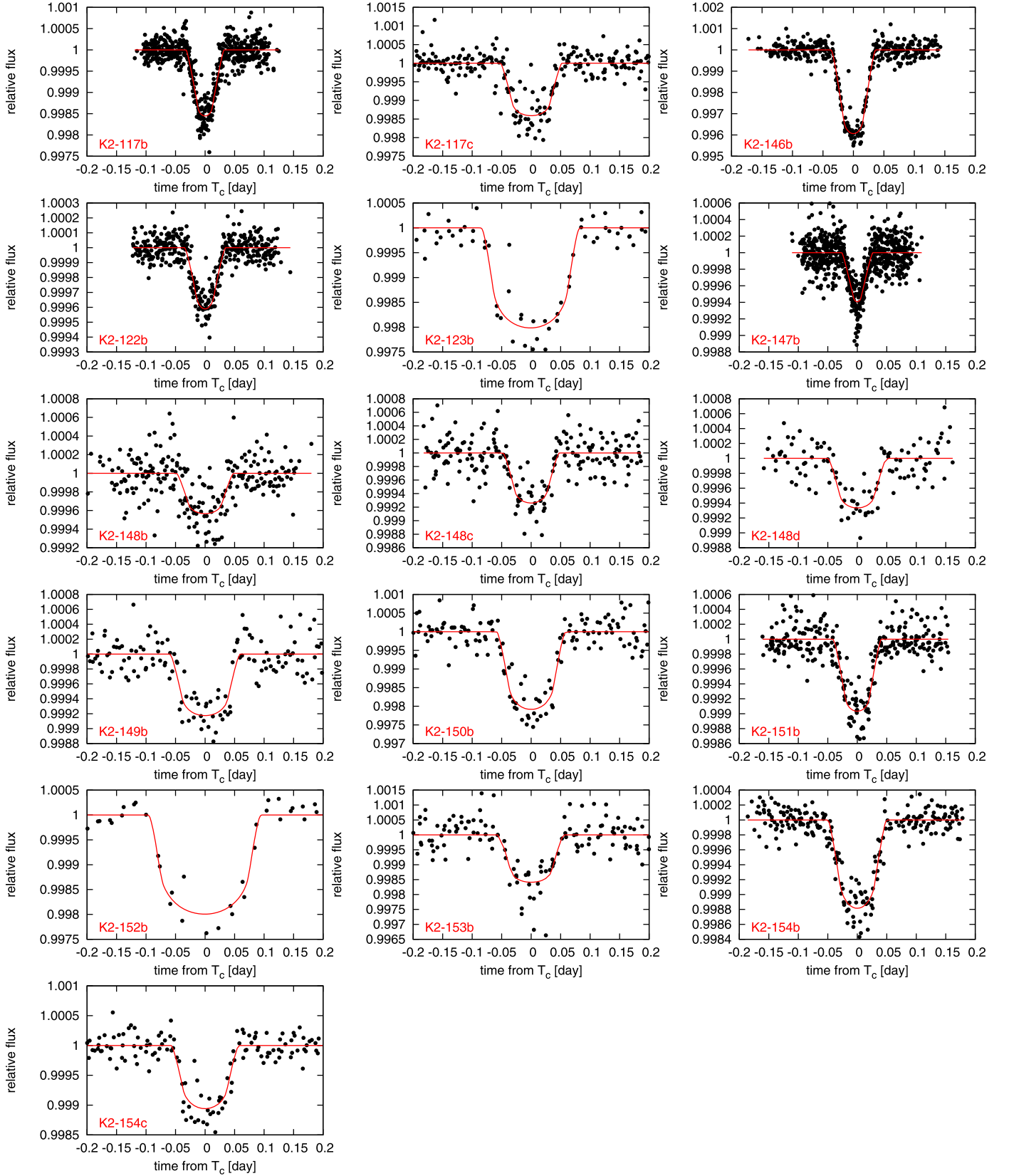
Figure 6. *K2* light curves around transits for individual candidates folded by their periods. Possible TTVs are corrected, and all transits are aligned in these light curves. For K2-148, the flux contamination from EPIC 220194953 is taken into account and the dilution factor is corrected. The best-fit transit curves are shown by the red solid lines.
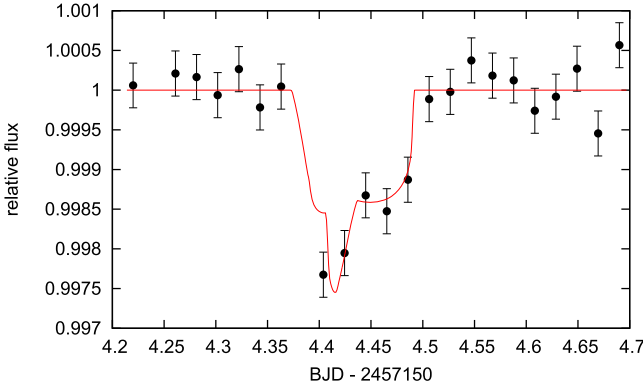
**Figure 7.** First double transit event observed for K2-117. The best-fit model is shown by the red solid line.
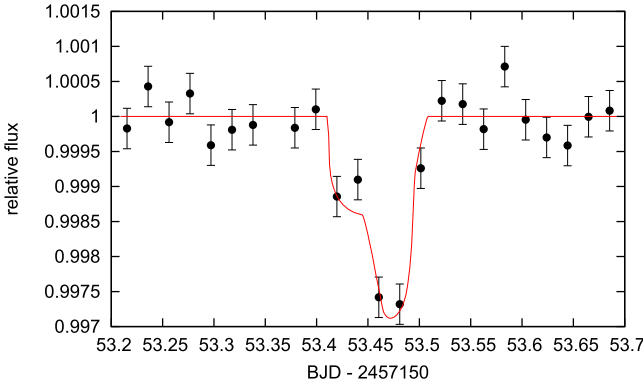
Figure 8. Second double transit event observed for K2-117. The best-fit model is shown by the red solid line.

day orbit with a possible TTV. We have performed a global fit to the *K2* light curve allowing every transit center to float freely, and confirmed the TTV as shown in Figure 9. As a result of inputting the TTV-corrected transit curve to vespa, we were able to validate K2-146b as a bona fide planet. The strong TTV (>30 minutes) suggests that the object causing TTV is either a very massive planet or has an orbit very close to the mean motion resonance (MMR), although detailed TTV modeling is beyond the scope of this paper.

K2-146 also exhibits the deepest transit among our sampled stars, making it a very unique target for atmospheric characterizations and TTV modeling by transit follow-ups from the ground and space. However, the predicted transit times are now highly uncertain due to the TTV combined with the long time interval after the *K2* observation, and it would be required to cover a long baseline around predicted transits. Fortunately, K2-146 is supposed to be observed by *K2* again in Campaign field 16, through which we can refine the ephemeris and possibly put a constraint on the object inducing the TTV.

K2-146 is very faint in the optical ($m_V = 16.2$ mag), but given the magnitudes in the near-infrared (e.g., $m_H = 11.6$ mag), one may be able to constrain the masses of K2-146b and the additional body by RV measurements with upcoming near-infrared spectrographs (e.g., IRD; Kotani et al. 2014). Adopting the empirical mass–radius relation for small planets by Weiss & Marcy (2014), the mass of K2-146b is estimated to be
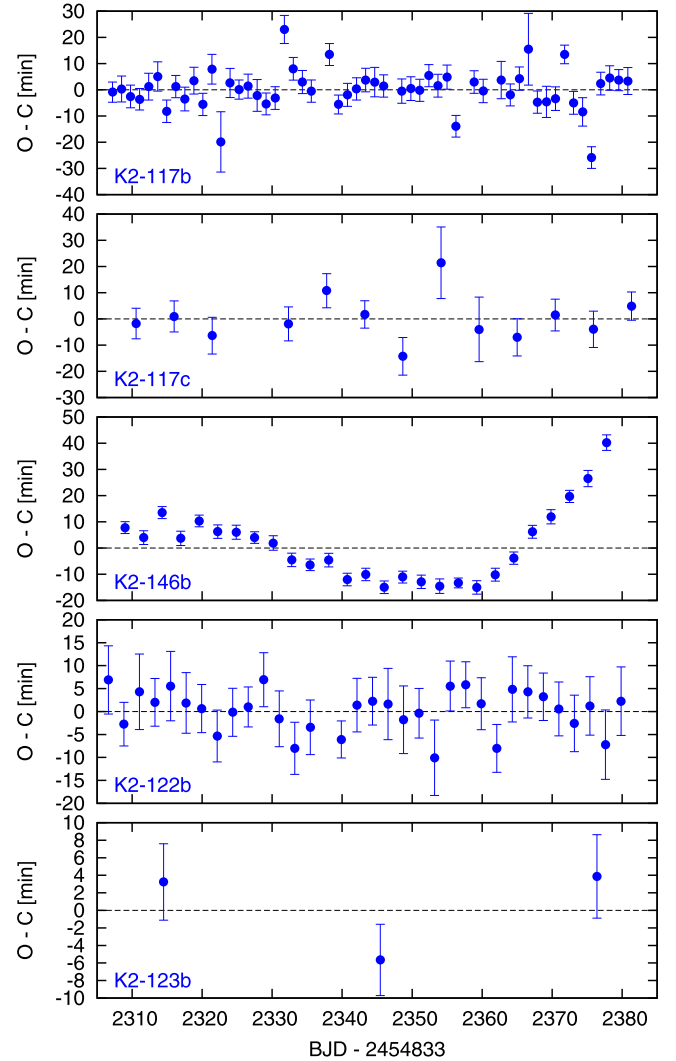
Figure 9. $O - C$ diagrams for mid-transit times for *K2* campaign field 5 planets.
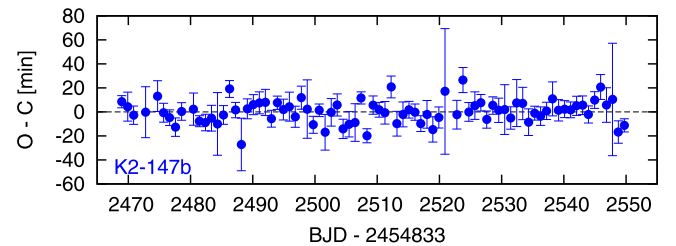
Figure 10. $O - C$ diagram for mid-transit times for K2-147b.

$\sim 5.6~M_\oplus$, and the corresponding RV semi-amplitude induced by this planet is $\sim 5.1~\mathrm{m\,s^{-1}}$.

5.3. K2-122

K2-122 is a quite metal-rich early M dwarf ([Fe/H] = 0.37 ± 0.12), hosting a close-in Earth-like planet ($R_p = 1.22~R_\oplus$, $P = 2.22$ days). Pope et al. (2016) reported this system to be a candidate planet host, which was later validated by Dressing et al. (2017b). In addition to an independent validation by AO imaging and high-resolution spectroscopy, we attempted a
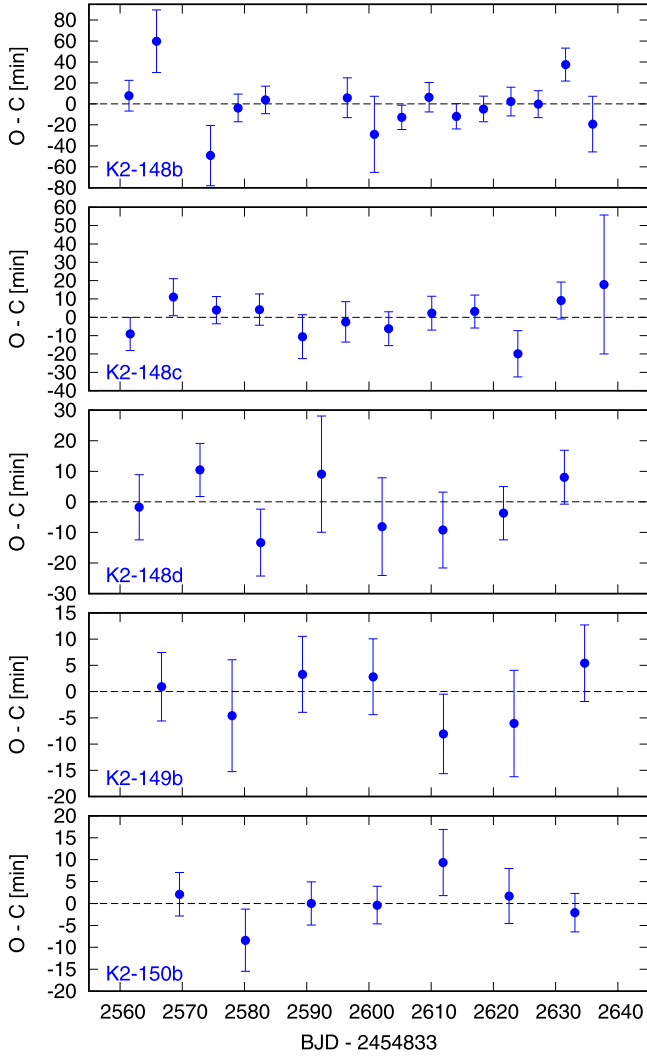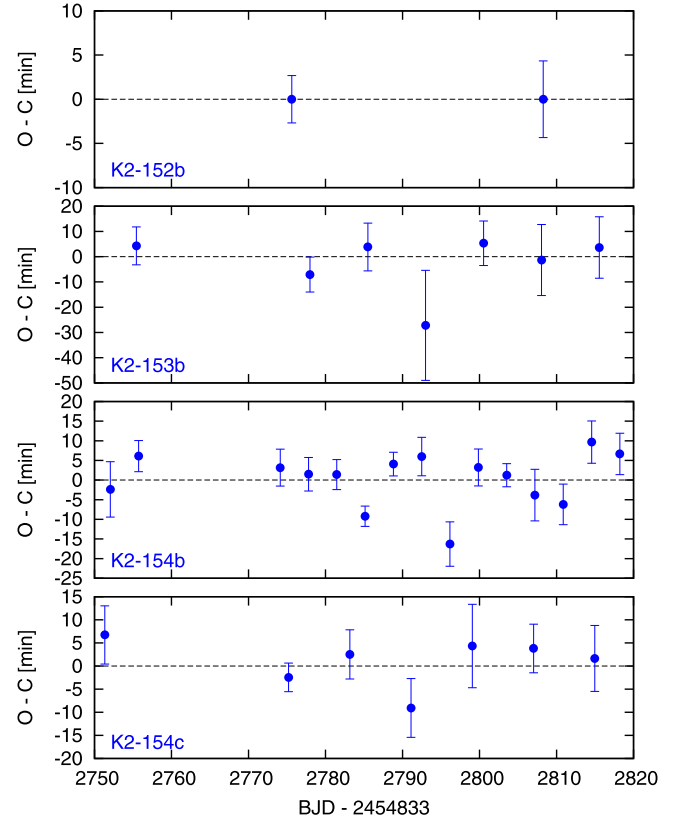
Figure 11. $O - C$ diagrams for mid-transit times for $K2$ campaign field 8 planets.

Figure 12. $O - C$ diagrams for mid-transit times for $K2$ campaign field 10 planets.

Table 5
Results of Follow-up Transit Observations for K2-151

Bandpass	R_p/R_s	T_c (BJD–2454833)
(MuSCAT observation)		2819.2215 ± 0.0015
g'	$0.0295^{+0.0070}_{-0.0098}$	
r'	$0.0360^{+0.0029}_{-0.0032}$	
z_s	$0.0312^{+0.0042}_{-0.0048}$	
(SIRIUS observation)		$2834.5651^{+0.0013}_{-0.0017}$
J	$0.0295^{+0.0070}_{-0.0098}$	
K_s	$0.0360^{+0.0029}_{-0.0032}$	

measurement of the planet mass. As shown in Figure 2, however, RVs measured by FIES and HARPS-N show a small variation. Assuming a circular orbit, we fit the observed RV data sets, for which we find the RV semi-amplitude of $K = -2.6 \pm 4.5 \text{ m s}^{-1}$. This is consistent with a non-detection, but the 1σ upper limit of K translates to ≈ 2.9 $M_\oplus$ for K2-122b's mass, suggesting that its composition may be somewhat similar to that of the Earth. Future monitoring with a greater number of RV points would allow for a more robust mass measurement.

5.4. K2-123

The detection of a transiting mini-Neptune ($R_p = 2.66$ $R_\oplus$) was reported around K2-123 by Pope et al. (2016), and Dressing et al. (2017b) later validated this planet. We have presented our own observations and data analysis including the precise RV measurement (Figure 2), and independently validated K2-123b as a genuine planet in a 31 day orbit.

The relatively large orbital distance ($a = 0.164$ au) translates to K2-123b's equilibrium temperature of 325 K on the assumption that its Bond albedo is 0.3 ($\sim$Earth's albedo). Thus, the planet is near the potential habitable zone, making it an attractive target for further characterizations. Given the moderate transit depth

($\sim$0.2%), the detection of transits is relatively easy with 2 m class ground telescopes, but one may have a small chance to observe a complete transit due to the long orbital period.

5.5. K2-147

K2-147 is a metal-rich M dwarf, orbited by a super-Earth with an ultrashort period (USP; $\sim$23 hr). No detection has so far been reported for this planet. According to exoplanet.eu,[30] K2-147b is the seventh validated USP planet ($P < 1$ day) around M dwarfs after Kepler-32f, Kepler-42c, Kepler-732c, KOI-1843.03 (Rappaport et al. 2013), K2-22b (Sanchis-Ojeda et al. 2015), and K2-137b (Smith et al. 2018). Interestingly, these planets show an increasing trend in R_p as a function of the orbital period P. We will later discuss the dependence of planetary sizes on insolation flux from host stars.

---

[30] http://exoplanet.eu/catalog
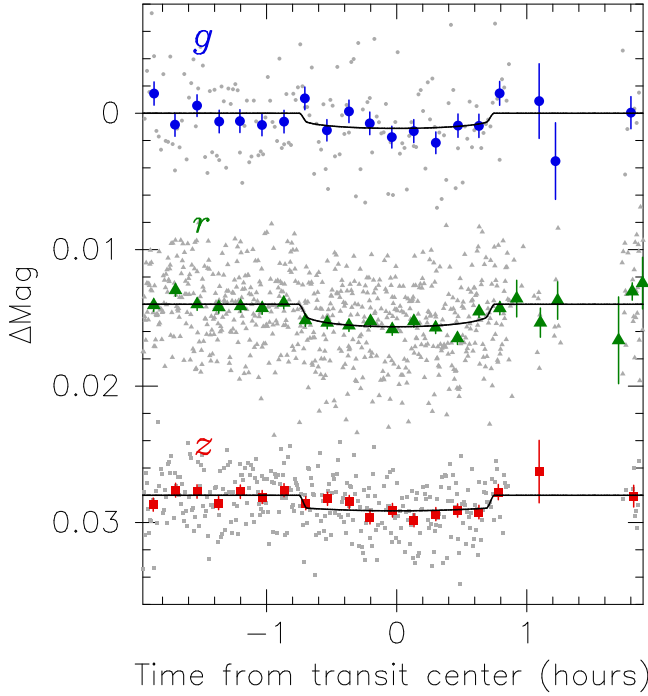
Figure 13. Ground-based transit observation for K2-151 by OAO/MuSCAT (gray dots). The binned flux data for the g', r', and z_s bands are shown by the blue circles, green triangles, and red squares, respectively. The black solid lines indicate the best-fit transit models for individual bands.
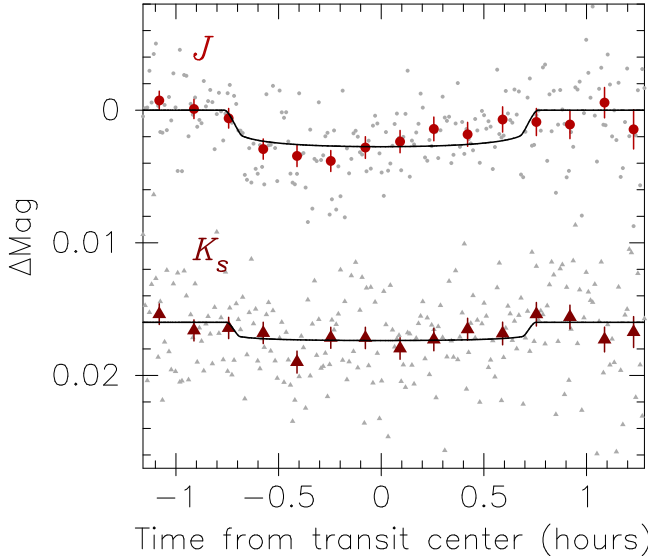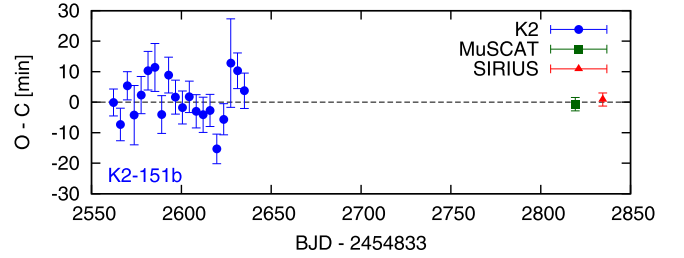

Figure 14. Ground-based transit observation for K2-151 by IRSF/SIRIUS (gray dots). The binned flux data for the J and K_s bands are shown by the dark red circles and brown triangles, respectively. The black solid lines indicate the best-fit transit models for individual bands.

5.6. EPIC 220187552

The transit-like signal was first detected for this target with a period of 17.09 days, and we measured its depth and duration to be 0.245% and 1.64 hr. As shown in Figures 3 and 4, however, EPIC 220187552 is comprised of at least two stars separated by $\sim 0\rlap{.}''3$. The transit curve is also V-shaped, and the preliminary light-curve fitting preferred a grazing transit. We thus conclude that either of the two stars seen in Figure 3 has an eclipsing stellar companion (a late M dwarf or a brown dwarf),
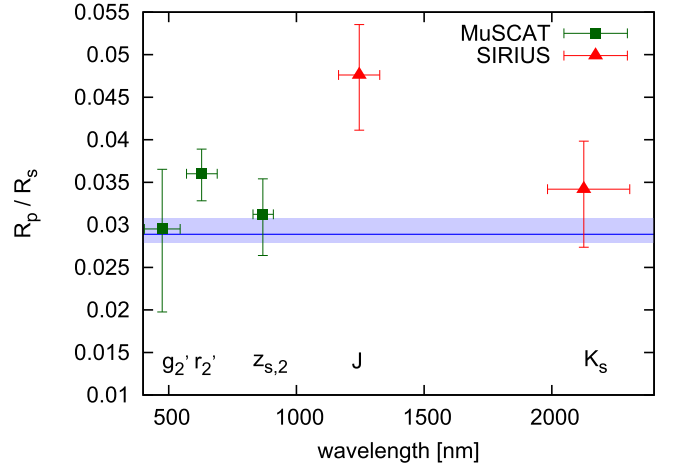
Figure 15. Observed R_p/R_s values of K2-151b in different bandpasses. The blue horizontal line and its upper and lower shaded areas indicate R_p/R_s and its $\pm 1\sigma$ errors in the K_p band.

Figure 16. $O - C$ diagram for mid-transit times for K2-151b. Ground-based transit observations are shown by the green square (MuSCAT) and red triangle (SIRIUS).

which is responsible for the relative Doppler shift in the cross-correlation profile (Figure 4). Indeed, as we described in Section 3.2, multiple spectra were obtained for this target by Subaru/HDS with the I_2 cell but the RV analysis did not converge, which is most likely because the observed spectra (with the I_2 cell) for RV measurement are different in shape from the template (without the I_2 cell), which complicates the fitting procedure.

In Figure 4, the two line positions in the cross-correlation profile are separated by $\Delta RV = 18\ \mathrm{km\,s^{-1}}$. The template spectrum for EPIC 220187552 was taken at JD $= 2457676.037$, which corresponds to the orbital phase of $\phi \sim 0.19$ when folded by the period of EPIC 220187552.01. This phase implies that the left line (RV $\sim 19\ \mathrm{km\,s^{-1}}$) in the cross-correlation profile corresponds to the star with a companion (i.e., EB), and the right one (RV $\sim 37\ \mathrm{km\,s^{-1}}$) corresponds to the other star. Assuming a circular orbit ($e = 0$) and the orbital inclination of $90°$ for the EB, we can roughly estimate the secondary-to-primary mass ratio q via

$$\Delta RV = 212.9083\left(\frac{M_1/M_\odot}{P/\mathrm{day}}\right)^{\frac{1}{3}} \frac{q}{(1+q)^{\frac{2}{3}}} \sin\phi\ (\mathrm{km\,s^{-1}}),\quad (2)$$

where M_1 is the mass of the primary star. When we adopt $M_1 = 0.6\,M_\odot$, we obtain $\sim 0.2\,M_\odot$ for the mass of the secondary. This would be easily confirmed by taking additional spectra for the absolute RV measurement. EPIC 220187552 provides a good testing bench, where high-resolution imaging and/or high-dispersion spectroscopy becomes powerful tools to identify and characterize hierarchical triple systems.

5.7. EPIC 220194953 and K2-148

As we have seen in Section 4.2.1, K2-148 turned out to host three planets, whose radii we estimate as 1.33 $R_\oplus$, 1.73 $R_\oplus$, and 1.64 $R_\oplus$ for the innermost ($P = 4.38$ days), middle ($P = 6.92$ days), and outermost ($P = 9.76$ days) planets, respectively. In order to see if EPIC 220194953 and K2-148 are bound to each other (common proper-motion stars), we checked the proper motions of the two stars and found (μ_α, μ_δ) = (-34.9 ± 6.8 mas yr^{-1}, -27.3 ± 7.7 mas yr^{-1}) and (-38.4 ± 9.4 mas yr^{-1}, -26.7 ± 3.1 mas yr^{-1}) for EPIC 220194953 and K2-148, respectively (Smart et al. 2013), indicating that the two stars share the same proper motion within the error bars. The almost identical RV values (Figure 4), along with the same distance (Table 3) to the stars, all imply that EPIC 220194953 and K2-148 are bound to each other. The separation of 9$\farcs$4 between the stars translates to the projected distance of $\sim$1100 au from each other. It is interesting that one of the two late-type stars in a wide-binary orbit has multiple super-Earths. Searching for planets around EPIC 220194953 also helps us understand the planet formation in cool wide-binary systems.

The period ratio of K2-148b and K2-148c is close to the 2:3 MMR. We investigated possible TTVs for the three planets, but no clear signal is seen in Figure 11, likely due to the small planetary masses.

5.8. K2-149

K2-149 is a slightly metal-rich early M dwarf, having a super-Earth ($R_p = 1.6 R_\oplus$) in an 11 day orbit. The RV measurement by Subaru/HDS shows no significant RV variation, supporting the planetary nature of K2-149b.

5.9. K2-150

The validated super-Earth K2-150b is similar to K2-149b in terms of its period ($P = 11$ days) and size ($R_p = 2.0 R_\oplus$), except that it is orbiting a cooler host star ($T_{\rm eff} = 3499$ K). Two absolute RVs were measured by Subaru/HDS, which are consistent within their errors. Given the moderate-depth transit ($\sim$0.2%) for a super-Earth, K2-150 is a good target for ground-based transit observations to refine system parameters and search for a possible TTV.

5.10. K2-151

K2-151 is a metal-poor M dwarf hosting a transiting small planet with $P = 3.84$ days. The size of K2-151b ($R_p = 1.35 R_\oplus$) suggests that it is likely a rocky planet. The relative brightness of the host star allowed us to observe the follow-up transits from the ground, enabling a considerable improvement in the transit ephemeris (Section 4.2.2). We also measured rough RVs, which completely ruled out the EB scenario. K2-151 is also a good target for future precise RV measurements in the near-infrared; with $m_J = 10.93$ mag, new and upcoming spectrographs like IRD and CARMENES (Quirrenbach et al. 2014) may be able to pin down the mass of K2-151b.

5.11. K2-152

The transiting mini-Neptune K2-152 is orbiting the host M dwarf every 33 days. Assuming a Bond albedo of $A_B = 0.3$, we estimate the equilibrium temperature of K2-152b to be $T_{\rm eq} = 331$ K, putting this planet near the habitable zone. The host star's brightness ($m_V = 13.73$ mag and $m_J = 10.96$ mag) and moderate transit depth ($\sim$0.2%) make this system a good target for further follow-ups, including precise RV measurements, either in the visible or near-infrared, and ground-based transit observations. Based on the mass–radius relation by Weiss & Marcy (2014), the mass of K2-152b is $\sim$7.0 $M_\oplus$, corresponding to the RV semi-amplitude of $K \sim 1.9$ m s^{-1}.

5.12. K2-153

We did not obtain multiple spectra for K2-153, which does not allow us to rule out completely the grazing EB scenario. Our HDS spectrum for K2-153, however, was taken at JD = 2457920.857, corresponding to $\phi \sim 0.23$, around which we expect to see the largest line separation in the spectrum if the transit signal is caused by an EB. We carefully inspected the secondary line in the cross-correlation profile, but found no evidence supporting the result of the vespa validation. K2-153 is a slightly metal-poor, early-to-mid M dwarf orbited by a super-Earth ($R_p = 2.0 R_\oplus$) with $P = 7.5$ days.

5.13. K2-154

We identified and validated two transiting mini-Neptunes ($R_p = 2.23 R_\oplus$ and 2.10 $R_\oplus$) around K2-154, a slightly metal-rich early M dwarf. The orbital periods are 3.68 and 7.95 days for K2-154b and K2-154c, respectively, whose ratio is somewhat close to the 2:1 resonance. We searched for TTVs for this system, but found no clear evidence as shown in Figure 12. A longer-term transit follow-ups with a better T_c precision would be required.

6. Discussion

All together, we have validated 16 planets around 12 of the low-mass stars observed by *K2*, based on high-resolution imaging and optical spectroscopy. Since the number of planets around M dwarfs has been increasing rapidly, thanks to *K2* and other projects, it is tempting to investigate the entire ensemble of M-dwarf planets, seeking patterns among their properties. We focus here on a search for any relationships between planet size, the stellar insolation (the flux received by the planet), and the stellar metallicity. This is because insolation and metallicity are strongly suspected of playing an important role in the formation and evolution of planets, and some possible correlations with planetary radius have already been discussed in the literature (e.g., Owen & Wu 2013; Buchhave et al. 2014; Dawson et al. 2015; Lundkvist et al. 2016).

To this end, we created a list of transiting planets around M dwarfs based on information in the NASA Exoplanet Archive,[31] exoplanet.eu, and exoplanets.org.[32] We restricted our sample to confirmed or validated planets around dwarf stars with $T_{\rm eff} \leqslant 4000$ K. We excluded unvalidated planet candidates. We also excluded six systems for which spectroscopic characterization is not available (Kepler-1350, 1582, 1624, 1628, 1646, and 1649).

For some systems, different investigators have reported different values for stellar and planetary parameters, sometimes differing by more than 3σ. For the sake of homogeneity, we adopted the stellar parameters of Mann et al. (2013a, 2013b, 2016a, 2016b, 2017a, 2017b) for a majority of the *Kepler* and

---

Table 6
Revised Spectroscopic Parameters Based on `SpecMatch-Emp`

System	$T_{\rm eff}$ (K)	[Fe/H] (dex)	R_s ($R_\odot$)
K2-3	3799 ± 70	-0.25 ± 0.12	0.500 ± 0.050
K2-5	4056 ± 70	-0.44 ± 0.12	0.607 ± 0.061
K2-9	3502 ± 70	-0.43 ± 0.12	0.358 ± 0.036
K2-18	3463 ± 70	0.01 ± 0.12	0.427 ± 0.043
K2-26	3680 ± 70	-0.06 ± 0.12	0.504 ± 0.050
K2-54	4012 ± 70	-0.18 ± 0.12	0.630 ± 0.063
K2-72	3393 ± 70	-0.49 ± 0.12	0.370 ± 0.037
K2-83	3806 ± 70	-0.05 ± 0.12	0.565 ± 0.057

Figure 17. Histogram of planet radius, for the validated and well-characterized transiting planets around M dwarfs. The number counts for mid-to-late M dwarfs are shown above those for early M dwarfs.

K2 stars in our sample, since those were derived based on the same (or similar) observing and reduction schemes. We also used the `SpecMatch-Emp` code to derive our own versions of the stellar parameters (Table 6), for cases where high-resolution spectra were available on the ExoFOP Web site.[33] As noted by Yee et al. (2017), the M-dwarf parameters derived by the `SpecMatch-Emp` code were calibrated using the sample of Mann et al. (2015), facilitating comparisons. For the other systems, for which high-resolution spectra were not available, we adopted the stellar parameters from the literature (Rojas-Ayala et al. 2012; Biddle et al. 2014; Berta-Thompson et al. 2015; Hartman et al. 2015; Torres et al. 2015; Hirano et al. 2016a; Dittmann et al. 2017; Dressing et al. 2017a; Gillon et al. 2017; Martinez et al. 2017), although no metallicity values were reported by Martinez et al. (2017). Planet radii were estimated based on the revised stellar radii and the values of R_p/R_s reported in the literature or by the *Kepler* team.

We split the sample into (1) planets around early M dwarfs (3500–4000 K) and (2) mid-to-late M dwarfs (<3500 K) to check for any differences in planet properties associated with stellar mass or effective temperature. By this definition, our sample consists of 96 planets around 63 early M dwarfs, and 32 planets around 17 mid-to-late M dwarfs.

Figure 17 shows the distribution of planet sizes on a logarithmic scale. A larger number of Earth-sized planets (0.5–1.25 $R_\oplus$) are found around the later-type stars, in spite of the smaller number of such stars in our sample. Although no completeness correction has been applied, it is interesting that Figure 17 shows that both types of stars have a deficit of planets with $R_p = 1.57$–$1.82 \, R_\oplus$, relative to somewhat smaller or larger planets. This is consistent with the findings of Fulton et al. (2017) and Van Eylen et al. (2017), based mainly on solar-type stars, that planets with sizes between 1.5–2 $R_\oplus$ are rarer than somewhat smaller or larger planets. This paucity has been interpreted as the outcome of photoevaporation on a population of planets with rocky cores ($\approx 1.5 \, R_\oplus$) with differing masses of gaseous envelopes and different levels of irradiation (Owen & Wu 2017), or as the outcome of the erosion of planetary envelopes by internal heat from cooling rocky cores (Ginzburg et al. 2017). The same sort of deficit seen in Figure 17 suggests that the same processes seem to be taking place around M dwarfs.

6.1. Insolation Dependence

Figures 18 and 19 display the planet radius as a function of stellar insolation S. In these figures, the red circles represent our newly validated planets, the blue squares are other *K2* planets,
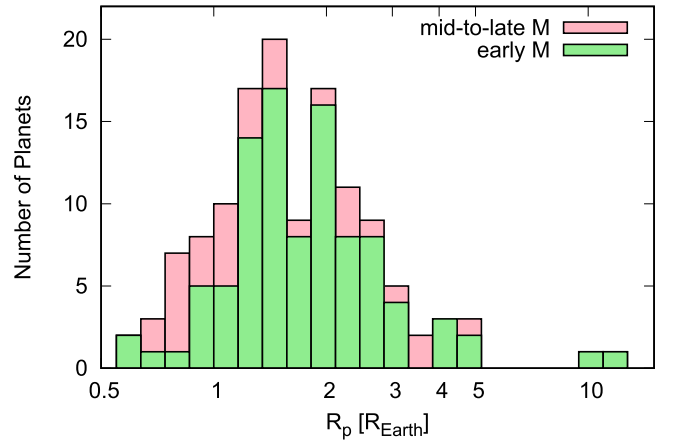
and the black triangles are the planets discovered during the primary *Kepler* prime mission or by ground-based surveys. Looking at Figures 18 and 19, we note that an important contribution of *K2* has been the discovery of relatively large planets ($R_p \gtrsim 2.5 \, R_\oplus$), which were not frequently detected during the *Kepler* primary mission.

Figures 18 and 19 show a lack of larger planets ($R_p \gtrsim 2 \, R_\oplus$) in the proximity of M stars. The deficit of close-in planets ($P \lesssim 2$ days) was previously reported by, e.g., Howard et al. (2012), Mazeh et al. (2016), and Fulton et al. (2017), mainly for solar-type stars. In order to draw a rough boundary above which planets are apparently rare, we took an approach similar to that described in Courcol et al. (2016) for the planet-mass versus stellar-metallicity diagram. Namely, we computed the cumulative weighted distribution of R_p for each insolation bin with its width being 0.2 in the log S space.[34] We then estimated the maximum radius for each bin by finding the 97% upper limit of this cumulative distribution. Finally, these upper limits were fitted with a linear function in the log $S - R_p$ space. We restricted this analysis to close-in planets ($P \lesssim 10$ days) and excluded hot Jupiters ($R_p > 8 \, R_\oplus$) since they seem to form a different population from their smaller counterparts (e.g., Mazeh et al. 2016).

The green line in Figure 18 represents this estimated boundary line. The moderate slope of the line ($R_p/R_\oplus = (-2.88 \pm 0.47) \log S/S_\oplus + (8.87 \pm 0.91)$) implies that only larger planets ($R_p \gtrsim 3 \, R_\oplus$) are missing in the proximity of the host stars. Owen & Wu (2013) showed that close-in low-mass planets are likely to suffer significant envelope evaporation due to the X-ray and extreme ultraviolet (EUV) radiation from the host star. On the other hand, theoretical works have shown that the gravitational potential of hot Jupiters is so deep that the XUV radiation from host stars cannot significantly strip their envelopes (e.g., Murray-Clay et al. 2009), which is consistent with the presence of the few hot Jupiters seen in Figure 18. Owen & Wu (2013) also noted that the evaporation of hydrogen envelopes should occur within the first 100 Myr, when stars are at the peak of their chromospheric activity. In this light, it is interesting that K2-33b seems to be unusually large for its level of current irradiation; the host is a pre-main-sequence star with an age of ≈ 11 Myr. This suggests that

[34] The bin size was set to 0.1 in log S, and thus each bin is overlapping with the neighboring bins.
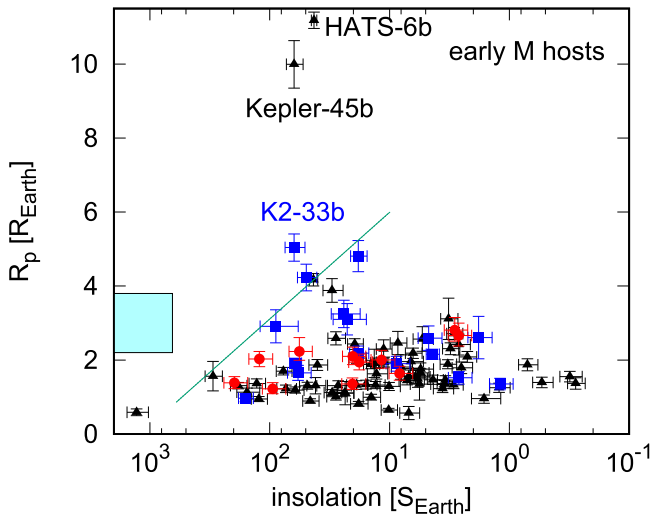
Figure 18. Stellar insolation fluxes vs. radii of planets around early M dwarfs (3500 K < T_{eff} ≤ 4000 K): our newly validated planets (red circles), other planets discovered by *K2* (blue squares), and planets from the *Kepler* primary mission and other surveys (black triangles). The cyan rectangle area is the "hot-super-Earth desert" described by Lundkvist et al. (2016). See the text for the upper boundary of R_p (green solid line).
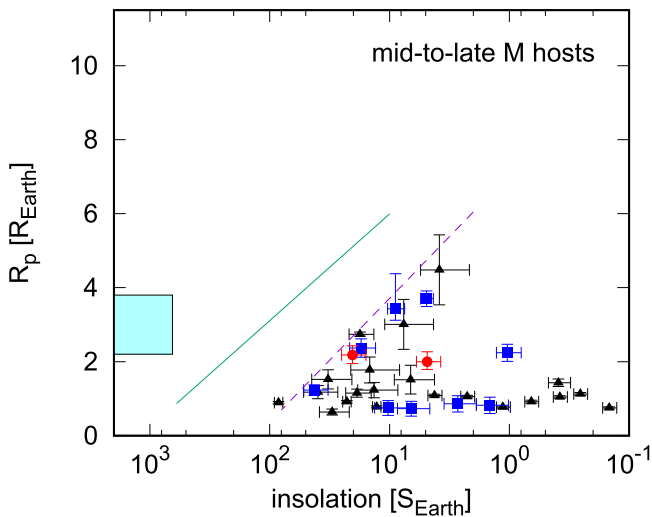
Figure 19. Stellar insolation fluxes vs. radii of planets around mid-to-late M dwarfs (T_{eff} ≤ 3500 K). Symbols and plot ranges are the same as in Figure 18.

K2-33b is actively evaporating and that its radius will shrink significantly over the next 100 Myr. Note that we did not exclude K2-33b from the analysis to draw the boundary.

The cyan rectangles in Figures 18 and 19 depict the "hot-super-Earth" desert discussed by Lundkvist et al. (2016) for close-in planets around solar-type stars (i.e., $2.2\,R_\oplus < R_p < 3.8\,R_\oplus$ and $S > 650\,S_\oplus$). Evidently, this rectangle is not a good description of the "desert" seen around M dwarfs. Instead, for M dwarfs, the "desert" seems to extend toward much lower insolation. Also interesting is that the observed "desert" is shifted toward lower insolation for the mid-to-late M stars. In Figure 19, we draw a similar upper boundary for R_p for the mid-to-late M sample by the purple dashed line. The derived slope of this boundary ($R_p/R_\oplus = (-3.34 \pm 0.34)\log S/S_\oplus + (7.05 \pm 0.42)$) agrees with that for the early M sample to within 1σ. To make this easier to see, the same green line that was drawn in Figure 18 is also drawn in Figure 19.

This result can be understood in the framework of Owen & Wu (2013), which implies that plotting the planet radius against the current bolometric insolation is not the most direct way to seek evidence for photoevaporation. Envelope evaporation is caused specifically by X-ray and EUV irradiation from the star and not by the bolometric flux. This is especially so for M dwarfs because they emit a higher fraction of X-rays relative to the bolometric flux than solar-type stars. Thus, planets around M dwarfs should have been eroded more efficiently relative to planets around solar-type stars with the same level of bolometric insolation. This was shown in Figure 7 of Owen & Wu (2013), wherein the lack of large planets extends to smaller bolometric fluxes for later-type stars. Owen & Wu (2013) also showed that when R_p is plotted against the empirically estimated X-ray exposure, the maximum planet size at a given X-ray exposure is approximately the same for all types of host stars. Although we do not attempt here to reproduce this type of plot, a comparison between Figures 18 and 19 does suggest a similar pattern. We note that this pattern is also compatible with the scenario in which photoevaporation is responsible for the radius gap (Figure 17) and favors photoevaporation over planetary internal heat as the explanation (Ginzburg et al. 2017), because in the latter case it should be the bolometric luminosity (not the XUV luminosity) that is relevant for atmospheric loss.

Another possible mechanism that could lead to a deficiency of close-in planets with large sizes is high-eccentricity migration (e.g., Rasio & Ford 1996; Nagasawa & Ida 2011) coupled with the disruption of planetary envelopes in the vicinity of the Roche limit (Matsakos and Königl 2016; Giacalone et al. 2017). Since Neptune-sized planets are often observed to have lower mean densities than Jovian or Earth-sized planets, their planetary envelopes should be relatively easy to strip. Mulders et al. (2015b) and Lee & Chiang (2017) suggested that the decline of the planet occurrence rate of all sizes at the shortest orbital distances ($P < 10$ days) could be the result of disk truncation at these orbital distances. Several mechanisms that truncate the planet populations around different types of stars are discussed in the literature (e.g., Plavchan & Bilinski 2013; Mulders et al. 2015b), including the tidal halting of migrating planets. The lack of planets of all sizes at higher insolation level in Figures 18 and 19 may also be consistent with this interpretation. In this picture, the disk truncation likely happens at a ≈2 day period for both early and mid-to-late M dwarfs to explain the lack of detected planets. However, the "truncation" we observed is not a vertical boundary in the insolation versus radius plane as one would expect in the disk truncation picture; instead, it has a moderate slope. In other words, at high insolation levels, there is only a lack of larger planets but not smaller planets. This would seem to favor the photoevaporation picture rather than the disk truncation picture.

Figures 18 and 19 also suggest a lack of large planets at low insolations (i.e., at longer orbital periods; $P \gtrsim 10$ days). This could be related to the formation process of these larger planets, which somehow is easier in their observed locations; the two figures illustrate that large planets including the hot Jupiters ($R_p \gtrsim 3\,R_\oplus$) seem to occur within a relatively narrow range of periods. However, given that the occurrence rate of planets with $R_p > 3\,R_\oplus$ is known to dwindle dramatically and long-period planets are more affected by detection biases associated with the transit geometry and short span of the *K2* monitoring,

it is premature to draw any conclusions on those outer planets. Compared to planetary systems around solar-type stars, little is known on the formation and evolution of M-dwarf planets, but measurements of eccentricity for close-in planets and other orbital parameters (e.g., the stellar obliquity) would help to test all these hypotheses for M-dwarf planets.

6.2. Metallicity Dependence

Stellar metallicity is also known to be related to planet size in exoplanetary systems (see, e.g., Buchhave et al. 2014). It is well-known that the occurrence rate of giant planets around solar-type stars depends sensitively on [Fe/H] (e.g., Johnson et al. 2010). The occurrence of Earth- and Neptune-sized planets were reported to be less dependent on metallicity (e.g., Sousa et al. 2008; Mayor et al. 2011), although some recent studies have shown that such planets are at least somewhat more frequent around metal-rich solar-type stars (e.g., Wang & Fischer 2015). In particular, there is growing evidence that small close-in planets ($P < 10$ days) are preferentially found around metal-rich stars (Mulders et al. 2016; Dong et al. 2017; Petigura et al. 2017a). Specifically, Wilson et al. (2017) derived the critical period, below which small planets orbit statistically metal-rich host stars ($P_{crit} \approx 8.3$ days).

Here we examine the relationship between R_p and [Fe/H] for M-dwarf planets, based on our new measurements and the parameters available in the literature. Previously, Schlaufman & Laughlin (2010) found a hint that planet-hosting M dwarfs are preferentially found in the region of the $(m_V - m_{K_s}) - M_{K_s}$ diagram where one expects metal-rich stars to be located. Rojas-Ayala et al. (2012) also investigated the metallicity of eight planet-hosting M dwarfs. They found that M-dwarf planets appear to be hosted by systematically metal-rich stars, and that Jovian planet hosts are more metal rich than Neptune-sized planet hosts. Mann et al. (2012), however, found no significant difference in $g - r$ color, a metallicity indicator, between the planet-candidate cool hosts and other cool stars. They ascribed the apparently high metallicity of cool planet-host stars reported in the literature to the contamination of the sample by misidentified giant stars.

Figures 20 and 21 show the radii of confirmed and validated transiting planets as a function of stellar metallicity for early M hosts (3500–4000 K) and mid-to-late M hosts (<3500 K). We restricted the sample to stars with spectroscopic measurements of [Fe/H]. For multiplanet systems, we have plotted only the largest planet. From these figures, we see that larger planets ($\gtrsim 3\,R_\oplus$) have only been found around metal-rich stars ([Fe/H] $\gtrsim 0.0$). This is similar to the situation with solar-type stars (Buchhave et al. 2012). Moreover, the mid-to-late M dwarfs seem to show a trend of increasing planet size with metallicity. For early M dwarfs, the correlation (if any) is not obvious; there are many small planets ($R_p \lesssim 2\,R_\oplus$) around supersolar metallicity stars. However, it must be remembered that these results have not been corrected for survey sensitivity. Transit surveys have a strong bias favoring the detection of short-period planets; there may be larger-radius planets that have been missed due to their longer periods. It is most significant that there are no detections of super-Neptune planets around metal-poor M dwarfs (the upper-left region in both figures), since such large planets are easier to detect than smaller planets.

Based on RV mass measurements for small planets around solar-type stars, it has been demonstrated that the observed
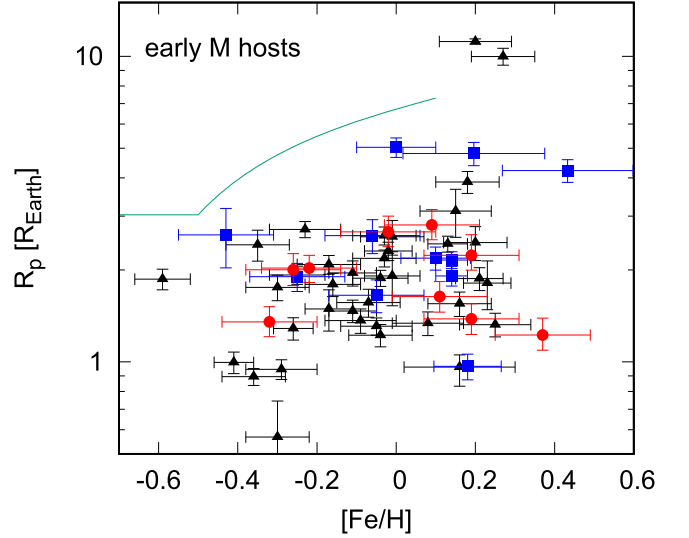
Figure 20. Host stars' metallicities from spectroscopy vs. radii of the planets around early M dwarfs (3500 K $< T_{eff} \leqslant 4000$ K). For multiplanet systems, the largest planets are plotted. Symbols are the same as in Figure 18. Note that contrary to Figures 18 and 19, the y-scale is logarithmic.
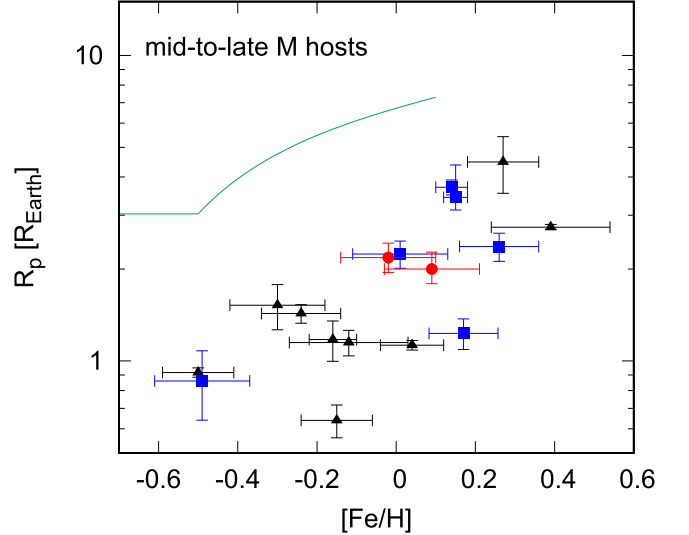
Figure 21. Host stars' metallicities from spectroscopy vs. radii of the planets around mid-to-late M dwarfs ($T_{eff} \leqslant 3500$ K). For multiplanet systems, the largest planets are plotted. Symbols are the same as in Figure 18.

maximum planet mass increases with metallicity (Courcol et al. 2016; Petigura et al. 2017b). A similar trend is seen for planet radius in Figures 20 and 21. To compare the previous finding with the distribution of M-dwarf planets, we draw in Figures 20 and 21 the upper envelope with the green solid line corresponding to Equation (1) of Courcol et al. (2016), where the planet mass is converted into radius assuming $R_p/R_\oplus \propto (M_p/M_\oplus)^{0.59}$ (Chen & Kipping 2017); all of the planets except hot Jupiters are below this line. Although the number of systems plotted is much smaller than in previous works for solar-type stars, the upper envelopes of the planet radius seem to be pushed toward lower values for coolest stars.

Dawson et al. (2015) advanced an explanation for the paucity of gaseous planets around metal-poor stars. They argued that metal-rich stars possessed protoplanetary disks with a higher surface density of solids, which led to more rapid formation of rocky cores with a critical mass ($>2\,M_\oplus$) for gas

accretion. If the formation timescale of critical-mass cores is longer than the disk lifetime, gaseous planets are unlikely to form. Although their argument focused on planets around solar-type stars, Figures 20 and 21 suggest that a similar argument might apply to low-mass stars.

To be more quantitative, we computed the Pearson's correlation coefficient r between R_p and [Fe/H]. We found $r = 0.332$ and 0.689 for early M and mid-to-late M stars, respectively, corresponding to the p-values of 0.0115 and 0.0022. This is evidence for some kind of relationship between planet radius and stellar metallicity for cool stars, as has been previously reported for solar-type stars (Buchhave et al. 2014). The mid-to-late M-dwarf sample shows a higher correlation coefficient than that of the early M sample, but the number of systems is also much smaller, which may have led to an apparently higher correlation by chance. To check whether the two samples are drawn from the same [Fe/H] − R_p distribution, we performed a Monte Carlo simulation in which 17 systems (the number of mid-to-late M systems) are randomly selected from the 57 early M dwarfs, and we computed the probability that the correlation coefficient r for the subset of 17 systems is higher than 0.689 (the observed r for the mid-to-late M stars). We found that its probability is 0.0063, implying that the mid-to-late M-dwarf sample indeed shows a stronger correlation between [Fe/H] and R_p.

Since the envelopes of close-in planets may have been evaporated (at least to some degree) by X-ray and EUV radiation from the star, we also tried to compute the correlation coefficients after removing planets for which the insolation exceeds 100 times the Earth's insolation, approximately the minimum value for which Figure 18 suggests that shrinkage takes place. We obtained a slightly higher correlation coefficient ($r = 0.352$) for the early M sample, but with an almost identical statistical significance ($p = 0.0114$), probably due to the smaller sample size. The R_p–[Fe/H] correlation is especially strong for the coolest M dwarfs ($T_{\rm eff} \leqslant 3500$ K), suggesting that the amount of initial solid material is extremely sensitive to the formation of Neptunian (and Jovian) planets with hydrogen–helium envelopes around the coolest stars.

Another relevant factor that affects the [Fe/H] − R_p relation is the correlation between the planet period and its host star's metallicity. Mulders et al. (2016) and Dong et al. (2017) have recently shown that stars with close-in rocky planets ($P <$ 10 days) are preferentially seen around metal-rich stars, and thus the [Fe/H] − R_p correlation could be in part affected by the [Fe/H]−P correlation. In order to examine such a correlation for M-dwarf planets, we split the whole sample (both early M and mid-to-late M samples) into inner planets ($P < 7$ days) and outer planets ($P > 7$ days), by which the two subsamples have approximately the same numbers of planets, and compared their mean metallicities. Consequently, we found a slightly higher mean metallicity for the inner-planet subsample ([Fe/H] = -0.033 ± 0.031) than for the outer-planet subsample ([Fe/H] = -0.084 ± 0.025), but in a statistically insignificant manner ($\approx 1.3\sigma$ difference). More planets are needed to confirm the [Fe/H] − P correlation.

Following Buchhave et al. (2014), we also computed the mean metallicity for our samples. We found the weighted mean metallicity to be [Fe/H] = -0.037 ± 0.010 for early M dwarfs, and 0.047 ± 0.017 for mid-to-late M dwarfs. Schlaufman & Laughlin (2010) noted that the mean metallicity of M dwarfs in the solar neighborhood is [Fe/H] ≈ -0.17. Therefore, our result

also indicates that the confirmed/validated planet-hosting M dwarfs have systematically high metallicities. The difference in the mean metallicities was also seen by Rojas-Ayala et al. (2012), but here we have extended their argument down to lower-mass stars and have used a larger number of well-characterized systems. We note, however, that unknown selection effects and/or different methodologies for metallicity measurements may have introduced biases in the mean metallicities in the two samples. Homogeneous measurements for volume-limited samples would be required to draw a firm conclusion.

There is no obvious reason why transit surveys should have a detection bias favoring high stellar metallicity, but there might be some effects. For instance, since M dwarfs with higher metallicity are more luminous than lower-metallicity counterparts for a given temperature, it may be somewhat easier to detect planet candidates and conduct follow-up observations for high-metallicity stars, leading to the validation of transiting planets, as we have done in the present paper. Given that we have included a variety of transiting planets detected by many space-based and ground-based surveys, it is not straightforward to account for any detection biases associated with stellar metallicity. We leave this for future work.

7. Conclusions

As part of our *K2* follow-up program (e.g., Sanchis-Ojeda et al. 2015), we have detected tens of planet candidates around M dwarfs in *K2* campaign fields 5–10, and conducted follow-up observations for candidate planets around M dwarfs. We have validated 16 transiting planets around 12 low-mass stars, out of which 12 are newly validated planets. All of the validated planets are relatively small in size (Earth-sized to mini-Neptunes), with periods ranging from 0.96 to 33 days. We have also identified a hierarchical triple system (EPIC 220187552) based on AO imaging and high-resolution spectroscopy.

We also reviewed the relationships between planet size, insolation, and metallicity that are emerging from the growing sample of M-dwarf planets. The planet-radius distribution suggested the same "gap" at around 1.5–2 $R_\oplus$ that was found by Fulton et al. (2017) for a larger sample of mainly solar-type stars. We saw an indication of the "desert" of very hot planets larger than about 2 $R_\oplus$, although for the coolest M stars, the desert begins at significantly lower insolation levels than for solar-type stars. We also confirmed that planets larger than about 3 $R_\oplus$ are preferentially seen around metal-rich stars ([Fe/H] > 0). Moreover, we found that the statistical significance of this trend is higher for the coolest M dwarfs. It will be important to try and corroborate these findings with a larger sample and after considering selection biases.

Fortunately, the *Transiting Exoplanet Survey Satellite* (Ricker et al. 2015) will be launched and will start the transit survey in the near future, which would make it more straightforward to deal with selection biases and extract the true distributions of stellar and planetary parameters with a larger number of sampled stars. To corroborate our findings, homogeneous characterizations of the systems with and without planets are essential.

Some of the new M-dwarf planets offer excellent prospects for further characterization, including Doppler mass measurement with optical or near-infrared spectroscopy (e.g., Kotani et al. 2014). As discussed above, the sizes of M-dwarf planets show some qualitative trends similar to those around solar-type

stars, but they also exhibit quantitatively different dependences on stellar insolation and metallicity. Perhaps the mass–radius relation for M-dwarf planets will also be seen to be different from that of planets around solar-type stars (Weiss & Marcy 2014). Measurements of orbital eccentricity and stellar obliquity could also provide helpful clues to the processes of planet formation and evolution around low-mass stars.

Software: IRAF (Tody 1986, 1993), ACORNS pipeline (Brandt et al. 2013), SpecMatch-Emp (Yee et al. 2017), EVEREST (Luger et al. 2016, 2017), PHOENIX (Allard et al. 2013), vespa (Morton 2015b), pyfits (Barrett et al. 2012).

ORCID iDs

Teruyuki Hirano ⃝ https://orcid.org/0000-0003-3618-7535
Fei Dai ⃝ https://orcid.org/0000-0002-8958-0683
Davide Gandolfi ⃝ https://orcid.org/0000-0001-8627-9628
Akihiko Fukui ⃝ https://orcid.org/0000-0002-4909-5763
Michael Endl ⃝ https://orcid.org/0000-0002-7714-6310
William D. Cochran ⃝ https://orcid.org/0000-0001-9662-3496
Tsuguru Ryu ⃝ https://orcid.org/0000-0002-1978-4883
Oscar Barragan ⃝ https://orcid.org/0000-0003-0563-0493
Juan Cabrera ⃝ https://orcid.org/0000-0001-6653-5487
Hans Deeg ⃝ https://orcid.org/0000-0003-0047-4241
Philipp Eigmüller ⃝ https://orcid.org/0000-0003-4096-0594
Malcolm Fridlund ⃝ https://orcid.org/0000-0003-2180-9936
Sascha Grziwa ⃝ https://orcid.org/0000-0003-3370-4058
Tomoyuki Kudo ⃝ https://orcid.org/0000-0002-9294-1793
Norio Narita ⃝ https://orcid.org/0000-0001-8511-2981
Grzegorz Nowak ⃝ https://orcid.org/0000-0002-7031-7754
Ignasi Ribas ⃝ https://orcid.org/0000-0002-6689-0312
Bun'ei Sato ⃝ https://orcid.org/0000-0001-8033-5633
Motohide Tamura ⃝ https://orcid.org/0000-0002-6510-0681
Vincent Van Eylen ⃝ https://orcid.org/0000-0001-5542-8870
Joshua N. Winn ⃝ https://orcid.org/0000-0002-4265-047X

References

Ahn, C. P., Alexandroff, R., Allende Prieto, C., et al. 2012, ApJS, 203, 21
Allard, F., Homeier, D., Freytag, B., et al. 2013, MSAIS, 24, 128
Alonso-Floriano, F. J. 2015, PhD thesis, Universidad Complutense de Madrid
Alonso-Floriano, F. J., Morales, J. C., Caballero, J. A., et al. 2015, A&A, 577, A128
Ballard, S., & Johnson, J. A. 2016, ApJ, 816, 66
Barrett, P., Hsu, J. C., Hanley, C., et al. 2012, PyFITS: Python FITS Module, Astrophysics Source Code Library, ascl:1207.009
Berta-Thompson, Z. K., Irwin, J., Charbonneau, D., et al. 2015, Natur, 527, 204
Biddle, L. I., Pearson, K. A., Crossfield, I. J. M., et al. 2014, MNRAS, 443, 1810
Bonfils, X., Delfosse, X., Udry, S., et al. 2013, A&A, 549, A109
Brandt, T. D., McElwain, M. W., Turner, E. L., et al. 2013, ApJ, 764, 183
Buchhave, L. A., Bizzarro, M., Latham, D. W., et al. 2014, Natur, 509, 593
Buchhave, L. A., Bakos, G. Á, Hartman, J. D., et al. 2010, ApJ, 720, 1118
Buchhave, L. A., Latham, D. W., Johansen, A., et al. 2012, Natur, 486, 375
Butler, R. P., Marcy, G. W., Williams, E., et al. 1996, PASP, 108, 500
Chen, J., & Kipping, D. 2017, ApJ, 834, 17
Ciardi, D. R., Crossfield, I. J. M., Feinstein, A. D., et al. 2017, arXiv:1709.10398
Claret, A., Hauschildt, P. H., & Witte, S. 2013, A&A, 552, A16
Clough, S. A., Shephard, M. W., Mlawer, E. J., et al. 2005, JQSRT, 91, 233
Cosentino, R., Lovis, C., Pepe, F., et al. 2012, Proc. SPIE, 8446, 84461V
Courcol, B., Bouchy, F., & Deleuil, M. 2016, MNRAS, 461, 1841
Crossfield, I. J. M., Ciardi, D. R., Petigura, E. A., et al. 2016, ApJS, 226, 7
Dai, F., Winn, J. N., Yu, L., & Albrecht, S. 2017, AJ, 153, 40
Dawson, R. I., Chiang, E., & Lee, E. J. 2015, MNRAS, 453, 1471
Díaz, R. F., Almenara, J. M., Santerne, A., et al. 2014, MNRAS, 441, 983
Dittmann, J. A., Irwin, J. M., Charbonneau, D., et al. 2017, Natur, 544, 333
Dong, S., Xie, J.-W., Zhou, J.-L., Zheng, Z., & Luo, A. 2018, AJ, 155, 10
Dressing, C. D., & Charbonneau, D. 2013, ApJ, 767, 95
Dressing, C. D., & Charbonneau, D. 2015, ApJ, 807, 45
Dressing, C. D., Newton, E. R., Schlieder, J. E., et al. 2017a, ApJ, 836, 167
Dressing, C. D., Vanderburg, A., Schlieder, J. E., et al. 2017b, AJ, 154, 207
Endl, M., & Cochran, W. D. 2016, PASP, 128, 094502
Evans, T. M., Aigrain, S., Gibson, N., et al. 2015, MNRAS, 451, 680
Frandsen, S., & Lindberg, B. 1999, in Astrophysics with the NOT FIES: A high resolution Fiber fed Echelle Spectrograph for the NOT, ed. H. Karttunen & V. Piirola (Piikkio: Univ. Turku, Tuorla Observatory), 71
Fridlund, M., Gaidos, E., Barragán, O., et al. 2017, A&A, 604, A16

Fukui, A., Livingston, J., Narita, N., et al. 2016, AJ, 152, 171
Fukui, A., Narita, N., Tristram, P. J., et al. 2011, PASJ, 63, 287
Fulton, B. J., Petigura, E. A., Howard, A. W., et al. 2017, AJ, 154, 109
Gandolfi, D., Barragán, O., Hatzes, A. P., et al. 2017, AJ, 154, 123
Gandolfi, D., Parviainen, H., Fridlund, M., et al. 2013, A&A, 557, A74
Giacalone, S., Matsakos, T., & Königl, A. 2017, AJ, 154, 192
Gillon, M., Triaud, A. H. M. J., Demory, B.-O., et al. 2017, Natur, 542, 456
Ginzburg, S., Schlichting, H. E., & Sari, R. 2017, arXiv:1708.01621
Girardi, L., Groenewegen, M. A. T., Hatziminaoglou, E., & da Costa, L. 2005,
    A&A, 436, 895
Guenther, E. W., Barragán, O., Dai, F., et al. 2017, A&A, 608, A93
Hartman, J. D., Bayliss, D., Brahm, R., et al. 2015, AJ, 149, 166
Hayano, Y., Takami, H., Oya, S., et al. 2010, Proc. SPIE, 7736, 77360N
Hirano, T., Fukui, A., Mann, A. W., et al. 2016a, ApJ, 820, 41
Hirano, T., Masuda, K., Sato, B., et al. 2015, ApJ, 799, 9
Hirano, T., Nowak, G., Kuzuhara, M., et al. 2016b, ApJ, 825, 53
Hirano, T., Sanchis-Ojeda, R., Takeda, Y., et al. 2014, ApJ, 783, 9
Howard, A. W., Marcy, G. W., Bryson, S. T., et al. 2012, ApJS, 201, 15
Howell, S. B., Sobeck, C., Haas, M., et al. 2014, PASP, 126, 398
Johnson, J. A., Aller, K. M., Howard, A. W., & Crepp, J. R. 2010, PASP,
    122, 905
Kirkpatrick, J. D., Henry, T. J., & McCarthy, D. W., Jr. 1991, ApJS, 77, 417
Kobayashi, N., Tokunaga, A. T., Terada, H., et al. 2000, Proc. SPIE,
    4008, 1056
Kotani, T., Tamura, M., Suto, H., et al. 2014, Proc. SPIE, 9147, 14
Kovács, G., Zucker, S., & Mazeh, T. 2002, A&A, 391, 369
Lee, E. J., & Chiang, E. 2017, ApJ, 842, 40
Luger, R., Agol, E., Kruse, E., et al. 2016, AJ, 152, 100
Luger, R., Kruse, E., Foreman-Mackey, D., Agol, E., & Saunders, N. 2017,
    arXiv:1702.05488
Lundkvist, M. S., Kjeldsen, H., Albrecht, S., et al. 2016, NatCo, 7, 11201
Mandel, K., & Agol, E. 2002, ApJL, 580, L171
Mann, A. W., Brewer, J. M., Gaidos, E., Lépine, S., & Hilton, E. J. 2013a, AJ,
    145, 52
Mann, A. W., Dupuy, T., Muirhead, P. S., et al. 2017a, AJ, 153, 267
Mann, A. W., Feiden, G. A., Gaidos, E., Boyajian, T., & von Braun, K. 2015,
    ApJ, 804, 64
Mann, A. W., Gaidos, E., & Ansdell, M. 2013b, ApJ, 779, 188
Mann, A. W., Gaidos, E., Lépine, S., & Hilton, E. J. 2012, ApJ, 753, 90
Mann, A. W., Gaidos, E., Mace, G. N., et al. 2016a, ApJ, 818, 46
Mann, A. W., Gaidos, E., Vanderburg, A., et al. 2017b, AJ, 153, 64
Mann, A. W., Newton, E. R., Rizzuto, A. C., et al. 2016b, AJ, 152, 61
Mann, A. W., Vanderburg, A., Rizzuto, A. C., et al. 2018, AJ, 155, 4
Marois, C., Lafrenière, D., Doyon, R., Macintosh, B., & Nadeau, D. 2006, ApJ,
    641, 556
Martinez, A. O., Crossfield, I. J. M., Schlieder, J. E., et al. 2017, ApJ,
    837, 72
Matsakos, T., & Königl, A. 2016, ApJL, 820, L8
Mayor, M., Marmier, M., Lovis, C., et al. 2011, arXiv:1109.2497
Mazeh, T., Holczer, T., & Faigler, S. 2016, A&A, 589, A75
Montet, B. T., Morton, T. D., Foreman-Mackey, D., et al. 2015, ApJ, 809, 25
Morton, T. D. 2015a, Isochrones: Stellar Model Grid Package, Astrophysics
    Source Code Library, ascl:1503.010
Morton, T. D. 2015b, VESPA: False Positive Probabilities Calculator,
    Astrophysics Source Code Library, ascl:1503.011
Morton, T. D., & Swift, J. 2014, ApJ, 791, 10
Mulders, G. D., Pascucci, I., & Apai, D. 2015a, ApJ, 798, 112
Mulders, G. D., Pascucci, I., & Apai, D. 2015b, ApJ, 814, 130

Mulders, G. D., Pascucci, I., Apai, D., Frasca, A., & Molenda-Żakowicz, J.
    2016, AJ, 152, 187
Murray-Clay, R. A., Chiang, E. I., & Murray, N. 2009, ApJ, 693, 23
Nagasawa, M., & Ida, S. 2011, ApJ, 742, 72
Nagayama, T., Nagashima, C., Nakajima, Y., et al. 2003, Proc. SPIE, 4841, 459
Narita, N., Fukui, A., Kusakabe, N., et al. 2015, JATIS, 1, 045001
Narita, N., Nagayama, T., Suenaga, T., et al. 2013, PASJ, 65, 27
Noguchi, K., Aoki, W., Kawanomoto, S., et al. 2002, PASJ, 54, 855
Ofir, A. 2014, A&A, 561, A138
Ohta, Y., Taruya, A., & Suto, Y. 2009, ApJ, 690, 1
Owen, J. E., & Wu, Y. 2013, ApJ, 775, 105
Owen, J. E., & Wu, Y. 2017, ApJ, 847, 29
Petigura, E. A., Marcy, G. W., Winn, J. N., et al. 2018, AJ, 155, 89
Petigura, E. A., Sinukoff, E., Lopez, E. D., et al. 2017b, AJ, 153, 142
Plavchan, P., & Bilinski, C. 2013, ApJ, 769, 86
Pont, F., Zucker, S., & Queloz, D. 2006, MNRAS, 373, 231
Pope, B. J. S., Parviainen, H., & Aigrain, S. 2016, MNRAS, 461, 3399
Press, W. H., Teukolsky, S. A., Vetterling, W. T., & Flannery, B. P. 1992,
    Numerical Recipes in C. The Art of Scientific Computing (2nd ed.;
    Cambridge: Cambridge Univ. Press)
Quirrenbach, A., Amado, P. J., Caballero, J. A., et al. 2014, Proc. SPIE, 9147,
    91471F
Rappaport, S., Sanchis-Ojeda, R., Rogers, L. A., Levine, A., & Winn, J. N.
    2013, ApJL, 773, L15
Rasio, F. A., & Ford, E. B. 1996, Sci, 274, 954
Ricker, G. R., Winn, J. N., Vanderspek, R., et al. 2015, JATIS, 1, 014003
Rojas-Ayala, B., Covey, K. R., Muirhead, P. S., & Lloyd, J. P. 2012, ApJ,
    748, 93
Sanchis-Ojeda, R., Rappaport, S., Pallè, E., et al. 2015, ApJ, 812, 112
Sanchis-Ojeda, R., & Winn, J. N. 2011, ApJ, 743, 61
Sato, B., Kambe, E., Takeda, Y., Izumiura, H., & Ando, H. 2002, PASJ,
    54, 873
Scalo, J., Kaltenegger, L., Segura, A. G., et al. 2007, AsBio, 7, 85
Schlaufman, K. C., & Laughlin, G. 2010, A&A, 519, A105
Shields, A. L., Ballard, S., & Johnson, J. A. 2016, PhR, 663, 1
Smart, R. L., Tinney, C. G., Bucciarelli, B., et al. 2013, MNRAS, 433, 2054
Smith, A. M. S., Cabrera, J., Csizmadia, S., et al. 2018, MNRAS, 474, 5523
Sousa, S. G., Santos, N. C., Mayor, M., et al. 2008, A&A, 487, 373
Suzuki, R., Kudo, T., Hashimoto, J., et al. 2010, in Proc. SPIE, 7735, 30
Tajitsu, A., Aoki, W., & Yamamuro, T. 2012, PASJ, 64, 77
Telting, J. H., Avila, G., Buchhave, L., et al. 2014, AN, 335, 41
Tody, D. 1986, Proc. SPIE, 627, 733
Tody, D. 1993, in ASP Conf. Ser. 52, Astronomical Data Analysis Software
    and Systems II, ed. R. J. Hanisch, R. J. V. Brissenden, & J. Barnes (San
    Francisco, CA: ASP), 173
Torres, G., Fressin, F., Batalha, N. M., et al. 2011, ApJ, 727, 24
Torres, G., Kipping, D. M., Fressin, F., et al. 2015, ApJ, 800, 99
Tull, R. G., MacQueen, P. J., Sneden, C., & Lambert, D. L. 1995, PASP,
    107, 251
Vanderburg, A., & Johnson, J. A. 2014, PASP, 126, 948
Vanderburg, A., Latham, D. W., Buchhave, L. A., et al. 2016, ApJS, 222, 14
Van Eylen, V., Agentoft, C., Lundkvist, M. S., et al. 2018, arXiv:1710.05398
Wang, J., & Fischer, D. A. 2015, AJ, 149, 14
Weiss, L. M., & Marcy, G. W. 2014, ApJL, 783, L6
Wilson, R. F., Teske, J., Majewski, S. R., et al. 2018, AJ, 155, 68
Winn, J. N., Holman, M. J., Torres, G., et al. 2008, ApJ, 683, 1076
Yee, S. W., Petigura, E. A., & von Braun, K. 2017, ApJ, 836, 77
Zacharias, N., Monet, D. G., Levine, S. E., et al. 2005, yCat, 1297, 0